Title
Functional optimality underpins the repeated evolution of the extreme “saber-tooth” morphology

Journal
Current Biology, 35(3)

ISSN
0960-9822

Authors
Pollock, Tahlia I
Deakin, William J
Chatar, Narimane
et al.

Publication Date
2025-02-01

DOI
10.1016/j.cub.2024.11.059

Article

Current Biology

Functional optimality underpins the repeated evolution of the extreme "saber-tooth" morphology

Graphical abstract

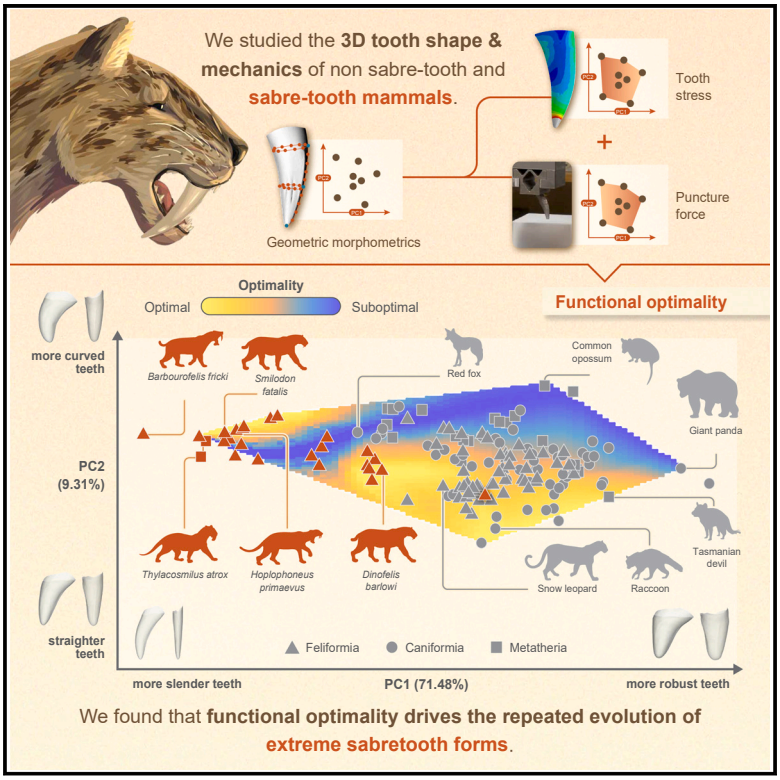

Highlights

- There is continuous morphofunctional diversity in saber-tooth canines
- Extreme saber teeth are optimal, enhancing puncture but reducing breakage resistance
- Functional optimality drives convergent evolution of extreme saber-tooth morphology
- Increased specialization of extreme saber forms may act as an evolutionary ratchet

Authors

Tahlia I. Pollock, William J. Deakin, Narimane Chatar, ..., Philip C.J. Donoghue, Emily J. Rayfield, Alistair R. Evans

Correspondence

tahliaipollock@gmail.com

In brief

Saber teeth are a classic example of convergence, having evolved repeatedly throughout mammalian history. Using 3D morphometrics, biomechanical testing, and a Pareto optimality analysis, Pollock et al. identify functional optimality as a key driver underpinning the repeated evolution of extreme saber-tooth morphologies.

Pollock et al., 2025, Current Biology *35*, 1–13
February 3, 2025
https://doi.org/10.1016/j.cub.2024.11.059

CellPress

Current Biology

CellPress
OPEN ACCESS

Article

Functional optimality underpins the repeated evolution of the extreme "saber-tooth" morphology

Tahlia I. Pollock,[1,2,10,11,13,*] William J. Deakin,[1] Narimane Chatar,[3,4] Pablo S. Milla Carmona,[1,11] Douglass S. Rovinsky,[5] Olga Panagiotopoulou,[6] William M.G. Parker,[2] Justin W. Adams,[7,8] David P. Hocking,[9] Philip C.J. Donoghue,[1,11] Emily J. Rayfield,[1,11] and Alistair R. Evans[2,8,12]

[1]Palaeobiology Research Group, University of Bristol, Bristol BS8 1QU, UK
[2]School of Biological Sciences, Monash University, Clayton, Melbourne, VIC 3800, Australia
[3]Department of Integrative Biology, UC Berkeley, Berkeley, CA 94720, USA
[4]UR Geology, Université de Liège, Liège 4000, Belgium
[5]Exhibitions, Australian Museum, Sydney, NSW 2010, Australia
[6]Department of Foundational Biomedical Sciences, Touro University California, Vallejo, CA 94592, USA
[7]Department of Anatomy and Developmental Biology, Monash Biomedicine Discovery Institute, Monash University, Clayton, Melbourne, VIC 3800, Australia
[8]Geosciences, Museums Victoria, Melbourne, VIC 3001, Australia
[9]Department of Zoology, Tasmanian Museum and Art Gallery, Hobart, TAS 7000, Australia
[10]X (formerly Twitter): @TIPollock
[11]X (formerly Twitter): @BristolPalaeo
[12]X (formerly Twitter): @EvansEvoMorph
[13]Lead contact
*Correspondence: tahliaipollock@gmail.com
https://doi.org/10.1016/j.cub.2024.11.059

SUMMARY

"Saber teeth"—elongate, blade-like canines—are a classic example of convergence, having evolved repeatedly throughout mammalian history. Within canine teeth, there is a trade-off between the aspects of shape that improve food fracture and those that increase tooth strength. Optimal morphologies strike a balance between these antagonistic functional criteria. The extreme saber-tooth morphology is thought to confer functional advantage for more specialized predatory adaptations and optimization; however, the adaptive bases underpinning their evolution remain unclear. To determine whether saber-tooth shape reflects selection for functionally optimal morphologies, we generated a morphospace of the 3D shape of 70 non-saber and 25 saber-tooth species, a subset of which were used to quantify functional metrics of puncture performance and breakage resistance. These data were combined using a Pareto rank-ratio algorithm to evaluate optimality. We demonstrate that extreme saber-tooth morphologies are functionally optimal, occupying a localized peak in our optimality landscape. Unlike other optimal canine morphologies, extreme saber teeth optimize puncture performance at the expense of breakage resistance. This identifies functional optimality as a key driver underpinning the repeated evolution of this iconic tooth.

INTRODUCTION

Hyper-elongate canines known as saber teeth are a classic example of convergence,[1,2] having evolved in mammals and mammalian precursors at least five times.[3–6] First appearing in the therapsid gorgonopsians ~265 million years ago in the Permian, this morphology has iteratively evolved in a range of carnivorous mammals, including metatherian sparassodonts like *Thylacosmilus*, the nimravid eutherian cat-like carnivorans, and true felids like *Smilodon*. These repeated instances of convergent evolution of the saber-tooth form are especially striking considering the significant shared morphological and structural modifications to the craniodental system required to accommodate it,[2,7] even to the point of breaking general rules of allometry,[8] indicating high adaptive value.

With no living representatives, there has been extensive debate over the likely predatory behavior(s) of saber-toothed taxa and how their extreme canines may have been used.[2,6,9–38] A wide-ranging body of work indicates that this dental morphotype is adapted for killing and taking down large prey.[2,10,39–41] This suggests that the saber-tooth morphology confers a functional advantage[6,24] for more specialized predatory adaptations and functional optimization.[6,7] Despite this, the underlying adaptive basis of this iconic tooth morphology remains poorly understood.[35] Previous studies are primarily based on morphological and biomechanical analyses of post-cranial[42–44] or cranial elements and integrated dentitions,[6,10,16,23,27,29,33–36,45] while very few have focused solely on the teeth in question: the canines.[13,25,37,46]

Canine teeth are often the first point of contact between predator and prey, being directly involved in prey acquisition and feeding.[47,48] In contrast to complex multi-part systems such as the craniodental system, the simple structure of canine teeth facilitates modeling and performance testing to a higher degree of

Please cite this article in press as: Pollock et al., Functional optimality underpins the repeated evolution of the extreme "saber-tooth" morphology, Current Biology (2024), https://doi.org/10.1016/j.cub.2024.11.059

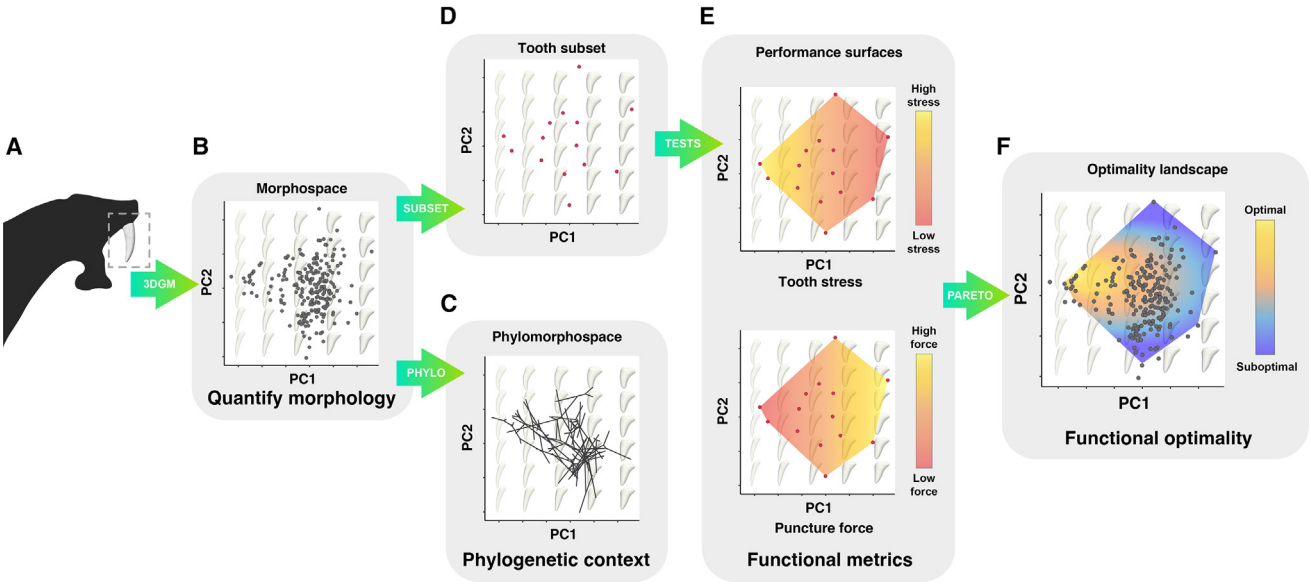

Figure 1. Workflow used in this study for landscape generation via a Pareto approach

(A) The 3D morphology of 235 canine teeth, representing 25 saber-tooth and 70 non-saber-tooth species, was captured via a geometric morphometrics approach (3D GMM).

(B) 3D GMM results were input into a principal component analysis (PCA) to generate a morphospace of canine tooth shapes.

(C) Mean shapes for upper teeth of each species were calculated, and to this, we added an informal time-scaled composite phylogeny to generate a phylomorphospace.

(D) From our morphospace, we selected a subset of 14 teeth, including saber-tooth and non-saber-tooth morphologies, that spanned a majority of the shape variation present to quantify functional metrics related to tooth performance.

(E) Physical tests were used to quantify puncture performance (maximum puncture force [N]), and finite-element analysis (FEA) was applied to model tooth stress (maximum von Mises stress [MPa]). Functional metrics from performance tests were input into the morphospace and interpolated to create two unique performance surfaces.

(F) These morphological and biomechanical data were then integrated via a Pareto rank-ratio algorithm[54] to generate an optimality landscape to pinpoint which tooth morphologies are functionally optimal.

precision and will allow the inference of functional capabilities and "optimal" forms. To perform effectively, a canine must fulfill two key criteria: (1) be sharp and slender enough to puncture food and (2) be blunt and robust enough to resist breakage.[49,50] However, there is a trade-off between the aspects of shape that improve food fracture and those that increase tooth strength. Such a trade-off appears to be universal among pointed structures designed to puncture.[51] Optimal tooth morphologies maximize these antagonistic functional criteria and will lie along a Pareto front[52–54] of shapes optimized for breakage resistance, puncture performance, or a trade-off between the two.

In this study, we elucidate the underlying adaptive basis of saber teeth by determining whether selection is driven toward functionally optimal morphologies in the face of antagonistic biomechanical relationships. We applied a landscape approach that integrates morphological and biomechanical data within a Pareto framework to assess optimality. Canine tooth shape was quantified via 3D geometric morphometrics (3D GMM) in a range of non-saber-tooth mammalian carnivores as well as extinct eutherian and metatherian saber-tooths. From the resulting morphospace, we selected a subset of teeth that spanned a majority of the shape variation present and subjected them to biomechanical analyses quantifying functional metrics of puncture performance and breakage resistance. Puncture performance was quantified via physical puncture tests, and finite-element analysis (FEA) undertaken to model tooth stress under a range of feeding scenarios. Performance surfaces generated from each functional metric enabled us to establish how changes in tooth morphology impacted performance, and when integrated via a Pareto rank-ratio algorithm,[54] assess whether tooth morphologies are functionally optimized for breakage resistance, puncture performance, or a trade-off between these two metrics (see Figure 1 for workflow). If saber teeth are adapted to these tasks, we expect they will occupy peaks of optimality that serve as "attractors" in our landscape,[1] explaining observed morphological convergence. This would identify functional optimality as a key driver underpinning the selection for the extreme saber-tooth morphology.

RESULTS

Saber-tooth morphology in the context of mammalian carnivores

From our 3D GMM analysis of 235 teeth, representing 70 non-saber and 25 saber-tooth species, the first two principal components (PCs) described the majority of variation in the sample (PC1 = 71.48%, PC2 = 9.31%, total 80.79%). PC1 primarily correlates with tooth robusticity and lateral compression with some curvature and PC2 with the degree of tooth curvature (Figure 2; Figure S1). Our phylomorphospace, based on a composite

Please cite this article in press as: Pollock et al., Functional optimality underpins the repeated evolution of the extreme "saber-tooth" morphology, Current Biology (2024), https://doi.org/10.1016/j.cub.2024.11.059

CellPress
OPEN ACCESS

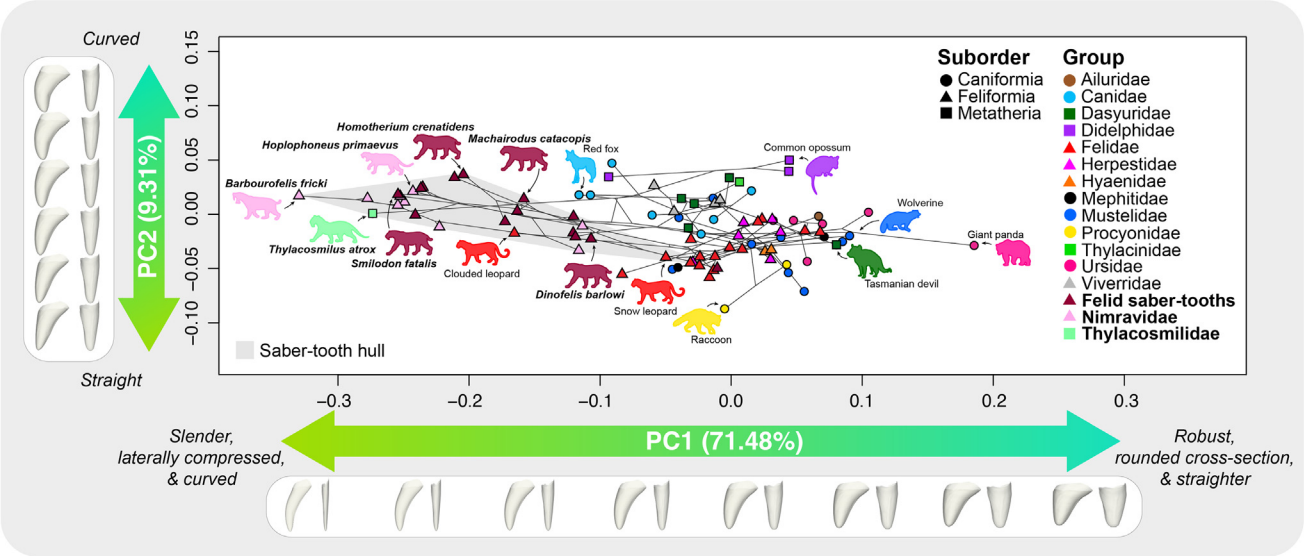

Figure 2. Phylomorphospace of canine teeth measured in this study

Generated via 3D geometric morphometrics, showing tooth shape variation among families and tooth types (non-saber-tooth and saber-tooth; indicated by saber-tooth hull). Ordination space is defined by the full canine tooth dataset (upper and lower canine teeth, total 235); however, for visualization purposes here we are showing upper canine tooth species mean shapes and an associated informal time-scaled composite phylogeny based on Slater and Friscia,[56] Rovinsky et al.,[57] and Barrett et al.[58] From PCA of Procrustes coordinates, PC1 explains 71.48% of the shape variation and is primarily correlated with tooth robustness, lateral compression, and some curvature, while PC2 explains 9.31% of the shape variation and is primarily correlated with curvature. See also Figure S1 and Data S1.

time-scaled phylogeny, shows that saber-toothed and non-saber-toothed taxa occupy distinct regions of morphospace, with some overlap. Based on our 3D shape analysis, saber-tooth morphological diversity is more complex than previously documented. We observe more of a continuum of saber-tooth morphologies compared with the traditional "dirk" and "scimitar" ecomorph classifications,[15–17,55] a pattern also captured in a recent 2D GMM analysis of saber-tooth canine morphology.[37]

Extreme, more derived morphologies are exemplified by *Smilodon*, *Barbourofelis*, *Hoplophoneus*, and *Thylacosmilus atrox*. Their canines are more slender and laterally compressed compared with other morphologies, while their curvature varies within the range observed for all teeth. Less extreme, more plesiomorphic morphologies are exemplified by *Dinofelis barlowi* and *Nimravus brachyops* and fall within the range of non-saber-tooth shapes. We also find saber-tooth shapes that are intermediate between the extreme and less extreme morphologies, for example, *Homotherium ischyrus*, *Machairodus catacopis*, and *Machairodus transvaalensis* or shapes like *Dinofelis piveteaui* that sit with the conical-toothed pantherine felids. Along this continuum of saber-tooth morphologies, teeth increase in slenderness, lateral compression, and curvature as they occupy increasingly more extreme regions of morphospace (middle left of the morphospace; Figure 2). Interestingly, we do not see shapes occupying other regions of extreme morphospace, for example, slender, less laterally compressed (rounder), and straighter morphologies (bottom left of the morphospace; Figure 2).

Saber-tooth morphology was surprisingly disparate even among the oldest taxa we have in our sample. The early Oligocene nimravids show highly derived extreme saber morphologies in *Eusmilus bidentatus* and *Hoplophoneus primaevus* alongside less extreme plesiomorphic sabers in *Nimravus brachyops* and *Pogodon platycopis*. We do not observe plesiomorphic sabers in later-branching nimravids. The later-occurring barbourofelins all exhibit highly derived sabers. Interestingly, Barbourofelini shows a trend through time toward more extreme derivation of the saber morphology, which occurs alongside an increase in body mass.[59] Indeed, the two latest-occurring taxa—the late Miocene *Barbourofelis loveorum* and *Barbourofelis fricki*—are the largest nimravids known and show the most derived saber morphology in our dataset. Within Felidae, there is no association observed between geological age and saber morphology, although that might change with denser sampling. However, the data are compatible with a link between phylogeny and saber shape. Early-branching felids like *Pseudaelurus* sp., Metailurini, and *Nimravides pedionomus* all show a less extreme plesiomorphic canine morphology that is more laterally compressed and curved compared with the typical "conical-toothed" extant felid canine. The remaining machairodontines—*Machairodus* spp., Homotherini, and Smilodontini—generally fall along a continuum of increasingly curved, slender, and laterally compressed sabers. Within Homotherini, the latest Miocene *Amphimachairodus palanderi* and the early Pleistocene *Homotherium ischyrus* both show less-derived sabers than their congeners. Interestingly, within felids, the less-derived saber morphologies were not lost to extinction until relatively recently. Both the plesiomorphic (e.g., *Dinofelis barlowi*) and the intermediate (e.g., *Machairodus transvaalensis*) saber shapes persisted alongside more derived morphologies into the Pleistocene.[37]

Our phylomorphospace and phenogram (Figure S1) show striking convergence on the extreme saber-tooth morphology

Please cite this article in press as: Pollock et al., Functional optimality underpins the repeated evolution of the extreme "saber-tooth" morphology, Current Biology (2024), https://doi.org/10.1016/j.cub.2024.11.059

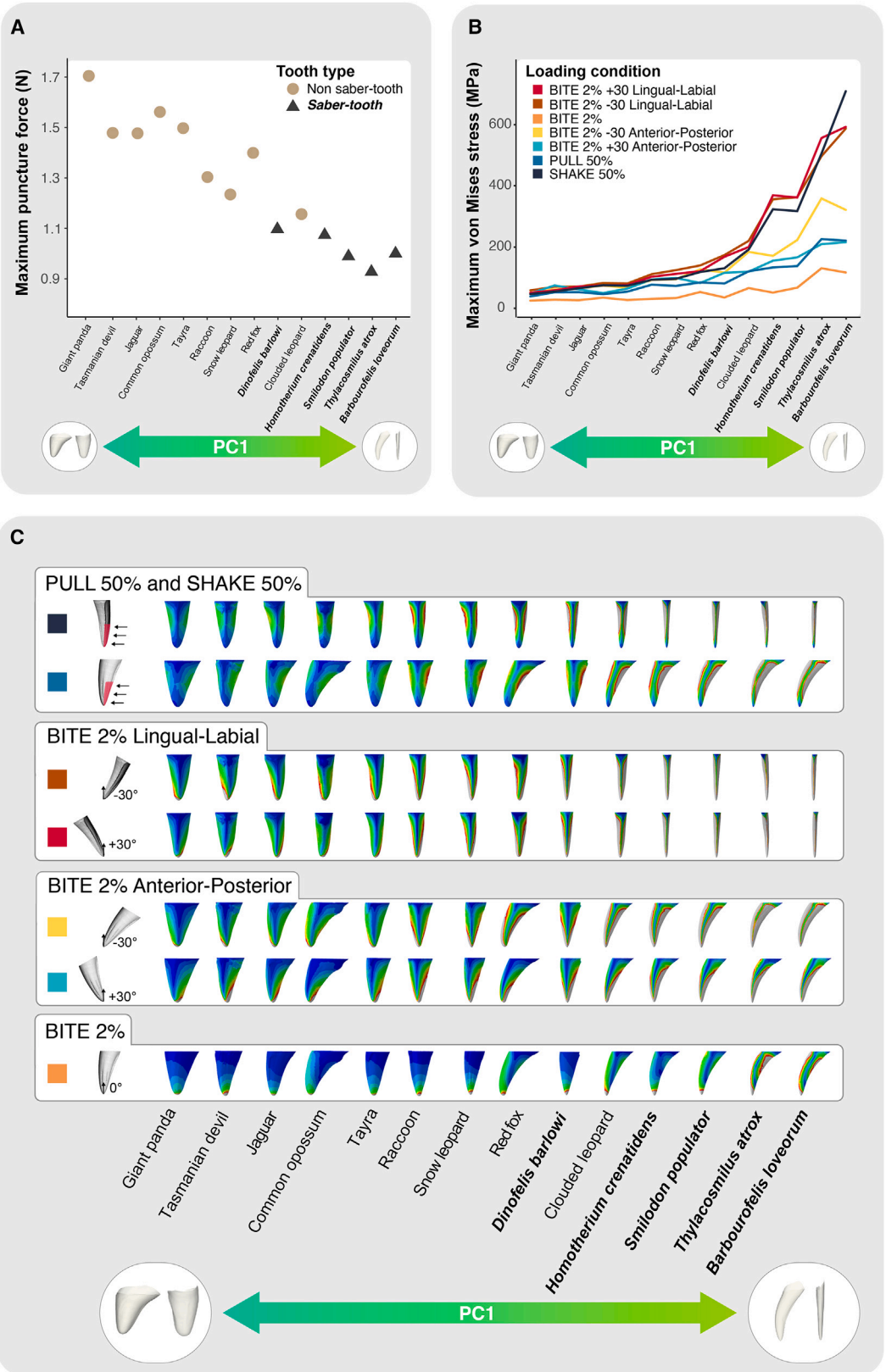

(legend on next page)

Please cite this article in press as: Pollock et al., Functional optimality underpins the repeated evolution of the extreme "saber-tooth" morphology, Current Biology (2024), https://doi.org/10.1016/j.cub.2024.11.059

among taxa that are separated by more than 120 million years,[60] with the metatherian *Thylacosmilus atrox* and eutherian *Barbourofelis* and *Smilodon* occupying a similar area of morphospace—a phenomenon also observed in previous studies of cranial convergence[6,22] and mandible morphology.[61]

Functional performance of saber teeth

Functional analyses were performed on a subset of 14 teeth that spanned a majority of the shape variation present in our morphospace. Tooth puncture force (N) was quantified as a proxy for puncture performance, using 3D-printed stainless steel models of teeth, which were scaled to the same surface area of 450 mm^2 (for compatibility with FEA and to enable integration of functional metrics in the downstream Pareto analysis [STAR Methods; Figure S2]). In a setup designed to mimic a tooth biting into prey, tooth models were driven into a block of gelatin substrate with known homogeneous material properties (Medical Gelatin #2, Humimic Medical, USA), and the force (N) and displacement (mm) were recorded over time. Puncture performance was inferred from the maximum force recorded for each simulated bite to a depth of 10 mm (to focus on initial puncture[62] and reduce the impact of tooth curvature [STAR Methods]). In this context, lower force values are associated with increased puncture effectiveness. Physical performance tests highlight the effectiveness of extreme saber-tooth morphologies, which recorded the lowest forces in the puncture experiments (Figure 3A). Less extreme saber-tooth shapes, like *Dinofelis barlowi*, along with non-saber-tooth shapes like the snow leopard (*Panthera uncia*), raccoon (*Procyon lotor*), and red fox (*Vulpes vulpes*) recorded intermediate forces. Non-saber-tooth morphologies like the giant panda (*Ailuropoda melanoleuca*), tayra (*Eira barbara*), and common opossum (*Didelphis marsupialis*) recorded the highest forces. The difference between the lowest (*Thylacosmilus atrox* = 0.93 N, *Smilodon populator* = 0.99 N, and *Barbourofelis loveorum* = 1.01 N) and highest (giant panda 1.70 N and common opossum 1.56 N) puncture forces indicates that the extreme saber-tooth morphology decreases the force required to puncture a ductile material by approximately 40%–50%, relative to robust non-saber-tooth shapes.

Tooth stress (von Mises stress [MPa]) was measured as a proxy for breakage resistance via FEA undertaken on scaled digital tooth models. We applied an established protocol from Pollock et al.[63] in which tooth models are constrained at their base and loaded to mimic predatory behaviors, including biting, pulling, and shaking (Figure S2; Pollock et al.[63]). Breakage resistance was inferred from the maximum von Mises stress calculated for a tooth model (calculated as the 90th percentile of von Mises stress [MPa] values for all surface nodes[63]). Higher von Mises stress values are associated with increased likelihood of breakage and decreased tooth strength. Finite-element simulations reveal the fragility of the extreme saber-tooth morphologies—*Smilodon populator*, *Barbourofelis loveorum*, and *Thylacosmilus atrox*—relative to less extreme saber-tooth and non-saber-tooth shapes. von Mises stresses among models show that extreme saber-tooth morphologies experience the highest stresses of all tooth models in each simulated feeding scenario (Figure 3B). This was also observed in the Shelbourne and Lautenschlager[37] analysis of saber-tooth canine morphology, which implemented 2D FEA. Less extreme saber-tooth morphologies like *Dinofelis barlowi* experienced stresses similar to non-saber-tooth shapes like the snow leopard, while the lowest stresses are observed in non-saber-tooth morphologies like the giant panda and the jaguar (*Panthera onca*). During biting, the difference between the highest (*Thylacosmilus atrox* = 125.64 MPa, *Barbourofelis loveorum* = 111.64 MPa, and *Smilodon populator* = 61.07 MPa) and lowest (giant panda 18.25 MPa and jaguar = 19.48 MPa) stress values indicates that extreme saber-tooth morphologies can experience approximately 300%–600% higher stresses than robust non-saber-tooth shapes. von Mises stress values among loading conditions within models reveal that almost all canine teeth experience higher stresses in shaking and lateral off-angle biting scenarios relative to biting and pulling. However, the magnitude of difference among scenarios is most pronounced in extreme saber-tooth morphologies (Figure 3B).

The trade-off between puncture performance and breakage resistance

Performance surfaces within our morphospace, generated from our functional metrics, illustrate the trade-off between puncture performance and breakage resistance[49] and demonstrate that the aspects of shape that decrease puncture force increase tooth stress, and vice versa. Specifically, as teeth become more slender and laterally compressed (increasingly negative values of PC1), stress increases while puncture force decreases (Figures 4A and 4B). From these performance surfaces, we derived predicted von Mises stress and puncture force values for all teeth in the morphospace that, when plotted against one another, form a performance space where it is possible to visualize the Pareto front of tooth morphologies (Figure 4C). The Pareto front represents the set of functionally optimal morphologies for which neither functional metric can be improved without deteriorating the performance of the other.[64]

To establish whether a particular tooth morphology favors relatively higher breakage resistance or puncture performance, we calculated an approximate weighting metric: the angle

Figure 3. Functional metrics of tooth performance

Measured on tooth subset representative of shape variation: giant panda (*Ailuropoda melanoleuca*) (USNM 258835), common opossum (*Didelphis marsupialis*) (USNM 578961), tayra (*Eira barbara*) (USNM 461839), red fox (*Vulpes vulpes*) (NMV C25074), clouded leopard (*Neofelis nebulosa*) (AMNH 22916), jaguar (*Panthera onca*) (AMNH 75462), snow leopard (*Panthera uncia*) (AMNH 35529), raccoon (*Procyon lotor*) (NMNH 265610), Tasmanian devil (*Sarcophilus harrisii*) (NMV C6242), and saber-tooth forms, *Dinofelis barlowi* (DNMNH TM 1542), *Smilodon populator* (NHMD ZMK 1/1845:2553), *Homotherium crenatidens* (MNHN PET2000a), *Barbourofelis loveorum* (UFV P27447), and *Thylacosmilus atrox* (FMNH P14531).

(A) Puncture performance was quantified as the maximum force (N) recorded for each model via a series of physical puncture tests with 3D-printed tooth models.

(B) Breakage resistance was quantified as the maximum von Mises stress in a range of predatory scenarios (biting, pulling, and shaking) via FEA undertaken on digital copies of tooth models.

(C) Stress magnitudes and distributions for each tooth model among predatory scenarios, shown in the lingual view. (A–C) Tooth models ordered (left to right) for increasingly negative PC1 values (increasing in slenderness and lateral compression). See also Data S2 and S3.

Please cite this article in press as: Pollock et al., Functional optimality underpins the repeated evolution of the extreme "saber-tooth" morphology, Current Biology (2024), https://doi.org/10.1016/j.cub.2024.11.059

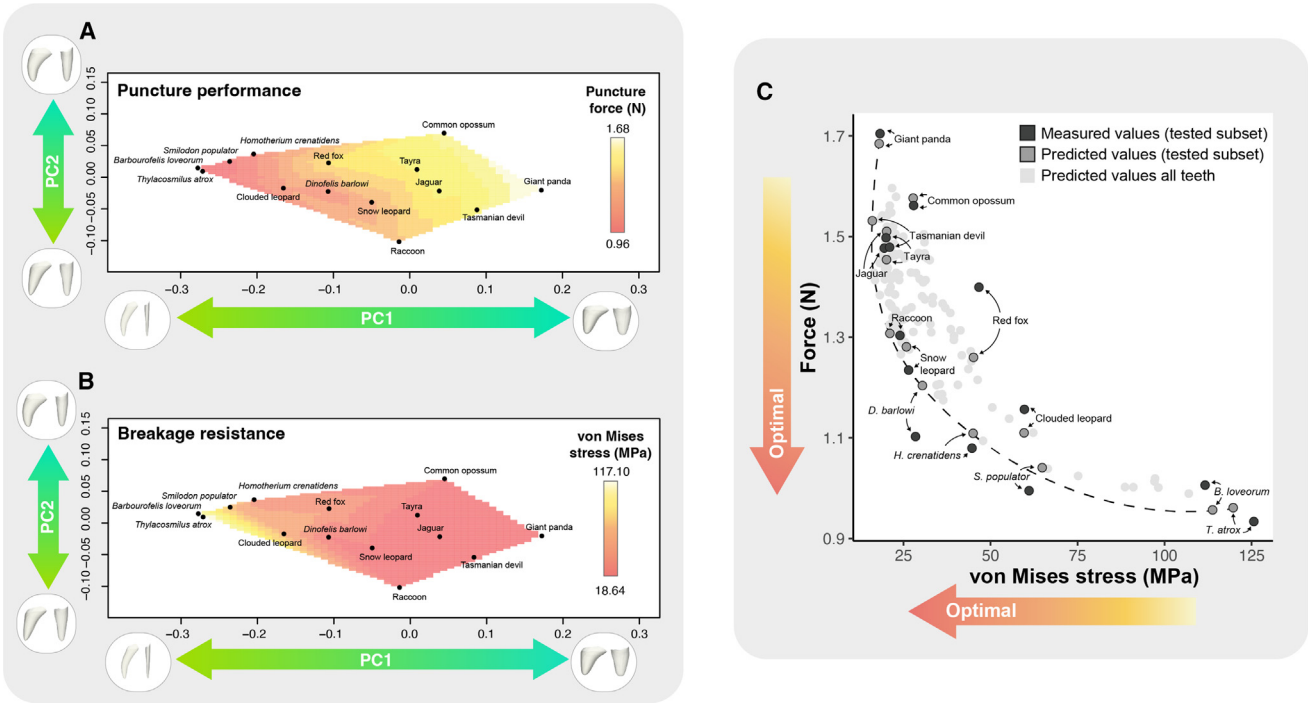

Figure 4. The trade-off between puncture performance and breakage resistance in canine tooth morphologies

(A and B) Performance surfaces generated from functional metrics related to tooth performance, which were interpolated from values measured for the tooth subset tested. The bounds of the surface hull are delineated by the subset of teeth tested. (A) Puncture performance (maximum force to puncture [N]) and (B) breakage resistance (maximum von Mises tooth stress [MPa] during biting).

(C) When plotted as von Mises stress (MPa) versus puncture force (N), measured values from the tested tooth subset (dark gray), those predicted from the performance surfaces for the tested tooth subset (lighter gray), and those predicted for the rest of the tooth dataset (lightest gray) build a performance space of tooth morphologies, where it is possible to visualize a Pareto front (dashed line): shapes for which neither metric can be improved without deteriorating the performance of the other. See also Data S3 and Figure S3.

between the x axis and the vector from the origin to each morphology's position in the performance space (STAR Methods). Higher angles indicate that a form is weighted toward breakage resistance, lower values favor puncture performance, and intermediate values a more balanced trade-off between metrics. We find that a higher proportion of tooth shapes lie in regions of performance space weighted toward breakage resistance, including morphologies like the giant panda, Tasmanian devil, European badger (*Meles meles*), raccoon, and wolverine (*Gulo gulo*) (top-middle left; Figure 4C; Figure S3). A smaller proportion is weighted toward a trade-off between breakage resistance and puncture performance, including less extreme saber-tooth shapes like *Dinofelis barlowi* and *Nimravus brachyops* (bottom left; Figure 4C; Figure S3). The smallest proportion of morphologies, which only includes the extreme saber-tooth morphologies like *Hopolophoneus*, *Smilodon*, and *Barbourofelis*, are weighted toward puncture performance (bottom right; Figure 4C; Figure S3). These approximate weights broadly concur with those calculated via the Dickson et al.[65] method (STAR Methods; Figure S3).

Saber-tooth morphologies are functionally optimal

To evaluate optimality and assess whether canine morphologies are optimized for breakage resistance, puncture performance, or a trade-off between metrics, our morphological and biomechanical data (represented as performance surfaces) were integrated via a Pareto rank-ratio algorithm, along with the assumptions: (1) low stress is preferable for breakage resistance and (2) low puncture force is preferable for puncture performance. The algorithm assigns each position in the morphospace a value from 0 to 1 (suboptimal to optimal), which, when plotted as the z axis above the morphospace, generates an optimality landscape.[54] Here we assume higher performance and optimality will result in higher fitness,[66] and so, like Deakin et al.,[54] areas of high optimality will have high adaptive value and areas of low optimality have low adaptive value. As our performance surfaces are generated using empirical tooth morphologies, not uniformly gridded theoretical forms, the resulting Pareto optimality landscape is more uneven than expected based on previous landscape studies[54,65,67–69] but still representative of the range of shapes present.

In our optimality landscape, we observe two distinct regions of higher optimality that correspond with different tooth morphologies (Figure 5). More "generalized" canines are represented by a range of straighter morphologies that vary in robustness and degree of lateral compression. These shapes occupy an area toward the lower middle of the morphospace, where we observe a moderate proportion of upper canine teeth, including the European badger and raccoon. This region also includes the less extreme saber-tooth morphologies, like *Dinofelis barlowi*,

Please cite this article in press as: Pollock et al., Functional optimality underpins the repeated evolution of the extreme "saber-tooth" morphology, Current Biology (2024), https://doi.org/10.1016/j.cub.2024.11.059

CellPress
OPEN ACCESS

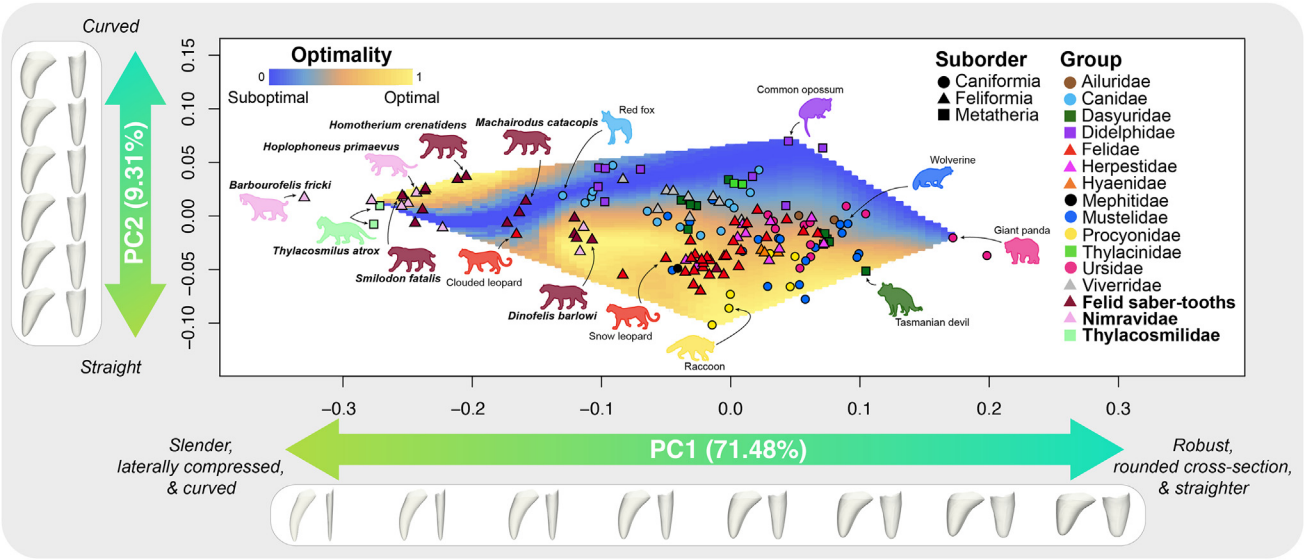

Figure 5. Optimality landscape derived from Pareto rank-ratio approach depicting functional optimality in the canine tooth morphospace

Ordination space is defined by the full canine tooth dataset (upper and lower canine teeth, total 235); however, for visualization purposes here we are showing only upper canine teeth. Optimality is derived from the Pareto rank-ratio algorithm[54] and shown as a surface, where warmer colors (yellow) highlight optimal morphologies (rank of 1) and cooler colors (blue) suboptimal morphologies (rank of 0). The bounds of the surface hull are delineated by the subset of teeth subjected to functional tests. See also Figures S3 and S6.

Nimravus brachyops, and *Pseudaelurus* sp., which are also optimal. Of additional note are the pantherine felids (including the snow leopard, tiger (*Panthera tigris*), lion (*Panthera leo*), and leopard (*Panthera pardus*), but excluding the jaguar), which sit slightly lower in the landscape in a region of morphospace associated with moderate-high values of optimality. The second region of high optimality in our landscape is occupied by more "specialized" canine shapes, which are slender, laterally compressed, and curved. Here, on a peak of optimality, we observe a majority of the extreme saber-tooth morphologies, including *Smilodon gracilis*, *Smilodon fatalis*, *Smilodon populator*, *Hoplophoneus primaevus*, and *Barbourofelis loveorum*. However, there are some saber-tooth morphologies that occupy areas of morphospace lower down the peak (moderate optimality), like *Barbourofelis morrisi* and *Albanosmilus whitfordi*. We also observe a valley of low optimality that separates our peaks of optimality (between extreme and less extreme saber-tooth shapes), which is occupied by the clouded leopard (*Neofelis nebulosa*) and intermediate saber-tooth morphologies like *Homotherium ischyrus*, *Machairodus catacopis*, and *Machairodus transvaalensis*. Additionally, we find that a large area of low optimality in our landscape is associated with more curved teeth of varying robusticity, like in the red fox, black-backed jackal (*Lupulella mesomelas*), thylacine (*Thylacinus cynocephalus*), and didelphids like the common opossum (*Didelphis marsupialis*) and Virginia opossum (*Didelphis virginiana*).

Our analysis demonstrates that both the extreme and less extreme saber-tooth morphologies are optimal, maximizing the antagonistic performance metrics related to puncture and breakage resistance. However, they are optimized in different ways: at one end of the continuum, less extreme plesiomorphic morphologies like *Dinofelis barlowi* are weighted toward the trade-off between puncture performance and breakage resistance, while at the other end, extreme derived morphologies, like *Barbourofelis loveorum*, are weighted toward puncture performance.

DISCUSSION

Based on functional analyses of teeth, we find support for the general consensus view that the more derived extreme saber-toothed predators were employing a killing bite that was directed toward the "softer" parts of their prey and distinct from the pantherine clamp-and-hold bite.[6,10,13,16,17,21,22,27,29] Puncture tests demonstrate that the extreme saber-tooth morphology can decrease the force required to puncture by up to a half, making them twice as effective when compared with robust canine morphologies (Figure 3A). Previous *in vivo* testing of pointed tooth forms shows that this is due to their slender, sharp shape, which decreases puncture force, especially for ductile and tough materials like the medical gelatin used in this study and vertebrate skin and muscle.[70–73] In such materials, applied force initially results in deformation, and cracks do not readily propagate.[72] These material properties underpin established form-function relationships in carnivore teeth between sharpness and the degree of carnivory,[11,70,74–77] and between slenderness and prey material properties.[75,77,78] Here, the sharper tips (Data S3) and more slender forms of the extreme saber-tooth morphologies facilitate lower puncture forces and suggest that they were biting into the ductile and tough materials like vertebrate flesh and likely directing their killing bite toward the softer parts of prey.

From our FEA, predatory scenarios that would reduce canine tooth stress and likelihood of breakage in extreme saber-tooth morphologies include biting into the softer parts of prey, a vertical bite or one that favors contact angles between tooth and prey that vary in the anterior-posterior direction, and limiting lateral loads

Please cite this article in press as: Pollock et al., Functional optimality underpins the repeated evolution of the extreme "saber-tooth" morphology, Current Biology (2024), https://doi.org/10.1016/j.cub.2024.11.059

like shaking or holding onto struggling prey. These scenarios favor a killing bite through penetration causing tissue damage and blood loss over the suffocation through clamp-and-hold bite of conical-toothed pantherine felids.[79] By contrast, less extreme saber-tooth morphologies, like *Dinofelis barlowi*, exhibit stresses and patterns of relative stress magnitudes closer to the conical-toothed snow leopard and may have employed a bite more similar to the pantherine clamp-and-hold. *Homotherium crenatidens* is intermediate between *Dinofelis* and *Barbourofelis* (Figure 3B), which may indicate a transitional killing method(s) between clamp-and-hold and canine penetration.[6,16,34]

Taken together, our functional analyses of saber teeth build a more complex picture of saber-tooth diversity, uncovering patterns similar to those found in recent studies highlighting continuous rather than dichotomous morphofunctional diversity among saber-toothed predators.[6,16,23,34,35,37] For teeth specifically, our 3D dataset provides greater morphofunctional detail than previous studies,[25,37,46] which allowed us to simulate the lateral loads that sabers may be exposed to (lingual-labial off-angle biting and shaking) as well as undertake puncture testing, which has never previously been achieved for saber teeth. Of additional note is that our 3D shape and FEA results broadly align with those obtained through 2D analyses.[37] This is likely due to the fact that the saber-tooth shape traits captured in 2D (slenderness and curvature) covary with those captured in 3D (lateral compression).

By evaluating the extreme saber-tooth morphology in an optimality framework, this study reveals that functionally optimal performance, within the context of a biomechanical trade-off between puncture performance and breakage resistance, likely underpins the evolution of this iconic tooth. We show that extreme saber-tooth morphologies exhibit a set of shape traits that distinguish them from other canine morphologies, exposing them to high stress in simulated predatory scenarios; however, it also allows them to puncture prey more effectively. Our optimality analysis shows that this morphology is maximizing the antagonistic functional criteria of puncture performance and breakage resistance, sitting atop a local peak in our landscape (Figure 5). Functional optimality may help to explain the exploration and occupation of this extreme area of the canine tooth morphospace and, more broadly, the repeated evolution of the extreme saber-tooth form. Following Conway Morris,[1] this area of optimal morphospace (design-space) is an adaptive peak that may be acting as an "attractor," driving morphology toward extreme saber-tooth phenotypes through selection of shapes with low breakage resistance but increasingly high puncture efficiency. We demonstrate that this form is one of the best solutions for the task of biting into ductile materials, and, according to Conway Morris,[1] such a solution will be repeatedly achieved through evolution by natural selection. We see this iterative evolution in this study, wherein we find several examples of morphological convergence atop a localized adaptive peak with multiple saber-toothed lineages moving toward the same solution.

However, our optimality analysis shows that to access this area of the morphospace, there is a valley of low optimality that must be crossed. In previous studies, valleys of low performance between adaptive peaks populated with intermediate morphologies have been associated with a trade-off between competing functional demands that select for different shape traits.[65,67–69,80,81] The Pareto rank-ratio approach tests for this; if intermediate shapes were optimized for the trade-off between performance metrics, they would appear optimal in our landscape. Between optimal regions in our morphospace (less extreme plesiomorphic saber-tooths-extreme derived saber-tooths), there appears to be a transition occurring, where the weighting between performance metrics changes, but not along the Pareto front. Regions of low optimality in our landscape may be due to several factors, chief among which is the possibility of functional demands or shape components not accounted for in our analysis. Specifically, the inputs of our Pareto analysis (performance metrics and 3D GMM data) only model unidirectional biting into a ductile material not hooking/pulling, shaking, or slicing prey, and our shape analysis does not capture tooth sharpness (tip or edge).[77] This is, in part, borne out when interrogating taxa in these regions of low optimality. For example, curved teeth exhibit low values of optimality and have been associated with hooking/pulling behaviors.[82–86] For saber-tooths, this may suggest that a shift in function occurs during the transition from more generalized, less extreme to specialized extreme morphologies (which has been suggested previously from studies of crania and mandibles[6,34,35]), and so other functional demands are relevant. Other possible explanations for regions of low optimality include constraints imposed by the structural properties of teeth,[87] tooth development,[88,89] evolutionary history,[90–92] or non-adaptive evolution.[93]

If the extreme saber-tooth form represents an optimal solution and has high adaptive value, it poses the question: why is this morphology not present in ecosystems today? Here we invoke the idea of the macroevolutionary ratchet,[7,80,94–96] which in the context of an adaptive landscape is akin to moving up the adaptive peak.[80,97] Previous research has shown that hypercarnivorous mammalian clades find it hard to retreat from their peak (from specialized to generalized morphologies) if ecosystem change occurs.[80,94,98–100] In this study we observe evidence of selection for an extreme morphology that is functionally specialized in a way that makes it vulnerable to changes in functional demands brought about by ecosystem upheaval within a single structure: the canine tooth. This phenomenon has been suggested for the saber-tooth morphotype in general, whereby the anatomical specializations that confer a capacity to hunt and kill large prey may have led to their extinction at times and locations when large prey became less abundant.[8,22,35,101] The pattern we observe in tooth morphology (e.g., increasingly extreme morphology through time in the Barbourofelini) is likely a key component that, cumulatively within the saber-tooth bauplan, increased extinction risk. This is supported by Piras et al.,[101] based on mandibles, which shows a pattern of decreasing diversification through time in saber-tooth groups and higher extinction rates relative to conical-toothed felids. This is in addition to Chatar et al.,[35] which shows a decrease in mandible and crania disparity through time as saber-toothed lineages occupy increasingly extreme regions of morphospace. However, it is important to note that not all saber-tooth groups in this study exhibited this pattern: within the machairodontines, we find that both the plesiomorphic less extreme and intermediate saber-tooth morphologies persist alongside the derived extreme morphology (e.g., *Dinofelis barlowi*, *Machairodus transvaalensis*, and *Smilodon* respectively) into the Pleistocene, which

may be evidence of niche partitioning among these groups,[6,16,34] a pattern also observed in recent studies of mandibles and crania[35] and teeth.[37] Regardless, the absence of the saber-tooth dental morphotype from the extant mammal assemblage emphasizes that the niche(s) they once occupied do not exist in the modern context.

Our study demonstrates the power of analyses of functional optimality for expounding the drivers of morphological diversity and convergence. In the context of saber teeth, our optimality landscape leverages the fundamental trade-off between puncture performance and breakage resistance. Using this framework, we reveal the adaptive basis that underpins the repeated evolution of an extreme morphology.

RESOURCE AVAILABILITY

Lead contact

Further information and requests for resources should be directed to, and will be fulfilled by, the lead contact, Tahlia Pollock (tahliaipollock@gmail.com).

Materials availability

This study did not generate new unique reagents.

Data and code availability

- The 3D surface file data of canine tooth models from extant taxa have been deposited at MorphoSource and are publicly available as of the date of publication in the project "Canine teeth of mammalian carnivores: the killer's toolkit" (https://www.morphosource.org/projects/000345195).
- The original 3D surface file data of canine tooth models from saber-toothed taxa have been deposited at MorphoSource and are publicly available as of the date of publication in the project "Functional optimality drives the repeated evolution of extreme saber-tooth forms" (https://www.morphosource.org/projects/000699335).
- The reconstructed 3D surface file data of canine tooth models from saber-toothed taxa in this paper will be shared by the lead contact upon request.
- The models designed for 3D printing have been deposited at Monash Bridges and are publicly available as of the date of publication in the project "Functional optimality underpins the repeated evolution of the extreme 'saber-tooth' morphology" (https://bridges.monash.edu/account/home#/projects/195548).
- The Abaqus project files (.cae) for all finite-element models have been deposited at Monash Bridges and are publicly available as of the date of publication in the project "Functional optimality underpins the repeated evolution of the extreme 'saber-tooth' morphology" (https://bridges.monash.edu/account/home#/projects/195548).
- All original code has been deposited at Monash Bridges in the project "Functional optimality underpins the repeated evolution of the extreme 'saber-tooth' morphology" (https://bridges.monash.edu/account/home#/projects/195548) and is publicly available as of the date of publication.

ACKNOWLEDGMENTS

For access to specimens, the authors wish to thank Guillaume Billet, Florent Goussard, and Christine Argot (MNHN, Paris, France); Benjamin Kear (PMU, Upssala, Sweden); Roula Pappa and Pip Brewer (NHMUK, London, United Kingdom); Patricia Holroyd (UCMP, Berkeley, USA); Samuel A. McLeod (NHMLA, Los Angeles, USA); Daniel Brinkman and Vanessa R. Rhue (YPM, New Haven, USA); Jin Meng, Judith Galkin, Ruth O'Leary, Eleanor Hoeger, Marisa Surovy, and Sara Ketelsen (AMNH, New York, USA); Nicholas Pyenson, Amanda Millhouse, Matthew Miller, Darrin Lunde, John Ososky, and Ingrid Rochon (USNM, Washington, DC, USA); Karen Roberts and Ricky-Lee Erickson (NMV, Melbourne, Victoria, Australia); Sandy Ingleby and Harry Parnaby (AMS, Sydney, NSW, Australia); and finally Kathryn Medlock and Belinda Bauer (TMAG, Hobart, Tasmania, Australia). For scanning of specimens, the authors would like to thank Hazel Richards, Anastasia Courtney, and Eliza Campbell (Monash University, Clayton, Australia); Jeanette Pirlo (UF, Gainesville, USA); Xiaoming Wang (NHMLA, Los Angeles, USA); and Kasper Lykke Hansen (Paleontological Collection at the Natural History Museum of Denmark, Copenhagen, Denmark). For collection of preliminary data, the authors wish to thank Astrid O'Connor (Monash University, Clayton, Australia). For 3D printing of tooth models, the authors would like to thank Bryce Melville, Aijun Huang, Tom Jarvis, and John Shurvinton (Monash University Centre for Additive Manufacturing, Clayton, Australia). For their expertise in facilitating and the setup of physical puncture tests, the authors wish to thank John Beadle (Department of Civil Engineering at Monash University). For sharing their time-scaled Maximum Clade Credibility tree of Feliformia (including Nimravidae and Felidae saber-tooths) phylogeny, the authors would like to thank Paul Z. Barrett.

This project was supported by a John Templeton Foundation Grant (JTF 62574) (to E.J.R. and P.C.J.D.; the opinions expressed in this article are those of the author and do not necessarily reflect the views of the John Templeton Foundation), Australian Research Council Discovery Project Grants (DP180101797 and DP230100613) (to A.R.E.), a Holsworth Wildlife Research Endowment - Equity Trustees Charitable Foundation & the Ecological Society of Australia Grant (to T.I.P.), a Monash University Post Publication Award (to T.I.P.), a Fonds de la Recherche Scientifique F.R.S.-FNRS Grant (FRIA FC 36251), and a BAEF postdoctoral fellowship and a National Science Foundation Grant (NSF DBI-2128146) (to N.C.). Additionally, Monash University Department of Anatomy and Developmental Biology and Biomedical Discovery Institute supported this project with funding for software (3-matic and Abaqus) (to O.P.).

AUTHOR CONTRIBUTIONS

Conceptualization, T.I.P. and A.R.E.; methodology, T.I.P. and A.R.E.; software, A.R.E., O.P., E.J.R., P.C.J.D., and P.S.M.C.; investigation, T.I.P., D.S.R., W.J.D., and W.M.G.P.; resources, A.R.E., N.C., and J.W.A.; visualization, T.I.P.; supervision, T.I.P., A.R.E., E.J.R., P.C.J.D.; writing – original draft, T.I.P.; writing – review & editing, T.I.P., W.J.D., N.C., P.S.M.C., D.S.R., O.P., W.M.G.P., J.W.A., D.P.H., P.C.J.D., E.J.R., and A.R.E.

DECLARATION OF INTERESTS

The authors declare no competing interests.

STAR★METHODS

Detailed methods are provided in the online version of this paper and include the following:

- KEY RESOURCES TABLE
- EXPERIMENTAL MODEL AND SUBJECT DETAILS
  - Dataset
  - Reconstruction
  - Study rationale
- METHOD DETAILS
  - 3D scanning and digitisation
  - Morphometric data collection (geometric morphometrics)
  - Phylogeny
  - Physical puncture tests
  - Finite element analysis
  - Pareto optimality rank-ratio approach
  - Tooth sharpness
  - Multi-material finite element analysis
- QUANTIFICATION AND STATISTICAL ANALYSIS
  - Canine tooth shape variation (geometric morphometrics)
  - Puncture performance
  - Breakage resistance
  - Performance surfaces and weighting metric
  - Canine tooth optimality landscape
  - Comparing landscape-based approaches

SUPPLEMENTAL INFORMATION

Supplemental information can be found online at https://doi.org/10.1016/j.cub.2024.11.059.

Received: September 30, 2024
Revised: November 5, 2024
Accepted: November 25, 2024
Published: January 9, 2025

REFERENCES

1. Conway Morris, S. (2003). Life's Solution: Inevitable Humans in a Lonely Universe (Cambridge University Press).
2. Emerson, S.B., and Radinsky, L. (1980). Functional analysis of sabertooth cranial morphology. Paleobiology *6*, 295–312. https://doi.org/10.1017/S0094837300006813.
3. Martin, L.D., Babiarz, J.P., Naples, V.L., and Hearst, J. (2000). Three ways to be a saber-toothed cat. Naturwissenschaften *87*, 41–44. https://doi.org/10.1007/s001140050007.
4. Dawson, M.R., Stucky, R.K., Krishtalka, L., and Black, C.C. (1986). *Machaeroides simpsoni*, new species, oldest known sabertooth creodont (Mammalia), of the Lost Cabin Eocene. Rocky Mountain Geology *24*, 177–182.
5. Van Valkenburgh, B., and Jenkins, I. (2002). Evolutionary patterns in the history of Permo-Triassic and Cenozoic synapsid predators. Paleontol. Soc. Pap. *8*, 267–288. https://doi.org/10.1017/S1089332600001121.
6. Lautenschlager, S., Figueirido, B., Cashmore, D.D., Bendel, E.-M., and Stubbs, T.L. (2020). Morphological convergence obscures functional diversity in sabre-toothed carnivores. Proc. Biol. Sci. *287*, 20201818. https://doi.org/10.1098/rspb.2020.1818.
7. Van Valkenburgh, B. (2007). Déjà vu: the evolution of feeding morphologies in the Carnivora. Integr. Comp. Biol. *47*, 147–163. https://doi.org/10.1093/icb/icm016.
8. Tamagnini, D., Michaud, M., Meloro, C., Raia, P., Soibelzon, L., Tambusso, P.S., Varela, L., and Maiorano, L. (2023). Conical and sabertoothed cats as an exception to craniofacial evolutionary allometry. Sci. Rep. *13*, 13571. https://doi.org/10.1038/s41598-023-40677-6.
9. Simpson, G.G. (1941). The Function of Saber-Like Canines in Carnivorous Mammals (American Museum of Natural History).
10. Akersten, W.A. (1985). Canine function in Smilodon (Mammalia; Felidae; Machairodontinae). Contrib. Sci. *356*, 1–22. https://doi.org/10.5962/p.226830.
11. Van Valkenburgh, B. (1988). Trophic diversity in past and present guilds of large predatory mammals. Paleobiology *14*, 155–173. https://doi.org/10.1017/S0094837300011891.
12. Vanvalkenburgh, B., and Hertel, F. (1993). Tough times at La Brea: tooth breakage in large carnivores of the late Pleistocene. Science *261*, 456–459. https://doi.org/10.1126/science.261.5120.456.
13. Biknevicius, A.R., Van Valkenburgh, B., and Walker, J. (1996). Incisor size and shape: implications for feeding behaviors in saber-toothed "cats". J. Vertebr. Paleontol. *16*, 510–521. https://doi.org/10.1080/02724634.1996.10011336.
14. Van Valkenburgh, B. (2008). Costs of carnivory: tooth fracture in Pleistocene and Recent carnivorans. Biol. J. Linn. Soc. *96*, 68–81. https://doi.org/10.1111/j.1095-8312.2008.01108.x.
15. Slater, G.J., and Van Valkenburgh, B. (2008). Long in the tooth: evolution of sabertooth cat cranial shape. Paleobiology *34*, 403–419. https://doi.org/10.1666/07061.1.
16. Figueirido, B., Lautenschlager, S., Pérez-Ramos, A., and Van Valkenburgh, B. (2018). Distinct predatory behaviors in scimitar- and dirk-toothed sabertooth cats. Curr. Biol. *28*, 3260–3266.e3. https://doi.org/10.1016/j.cub.2018.08.012.
17. Martin, L.D. (1989). Fossil history of the terrestrial Carnivora. In Carnivore Behavior, Ecology, and Evolution (Springer), pp. 536–568.
18. Duckler, G.L. (1997). Parietal depressions in skulls of the extinct sabertoothed felid *Smilodon fatalis*: evidence of mechanical strain. J. Vertebr. Paleontol. *17*, 600–609. https://doi.org/10.1080/02724634.1997.10011006.
19. Antón, M., and Galobart, À. (1999). Neck function and predatory behavior in the scimitar toothed cat *Homotherium latidens* (Owen). J. Vertebr. Paleontol. *19*, 771–784. https://doi.org/10.1080/02724634.1999.10011190.
20. Antón, M., Salesa, M.J., Pastor, J.F., Sánchez, I.M., Fraile, S., and Morales, J. (2004). Implications of the mastoid anatomy of larger extant felids for the evolution and predatory behaviour of sabretoothed cats (Mammalia, Carnivora, Felidae). Zool. J. Linn. Soc. *140*, 207–221. https://doi.org/10.1111/j.1096-3642.2003.00093.x.
21. Turner, A., Antón, M., Salesa, M.J., and Morales, J. (2011). Changing ideas about the evolution and functional morphology of Machairodontine felids. Estud. Geol. *67*, 255–276. https://doi.org/10.3989/egeol.40590.188.
22. Melchionna, M., Profico, A., Castiglione, S., Serio, C., Mondanaro, A., Modafferi, M., Tamagnini, D., Maiorano, L., Raia, P., Witmer, L.M., et al. (2021). A method for mapping morphological convergence on three-dimensional digital models: the case of the mammalian sabretooth. Palaeontology *64*, 573–584. https://doi.org/10.1111/pala.12542.
23. Chatar, N., Fischer, V., Siliceo, G., Antón, M., Morales, J., and Salesa, M.J. (2021). Morphometric Analysis of the Mandible of Primitive Sabertoothed Felids from the late Miocene of Spain. J. Mammal. Evol. *28*, 753–771. https://doi.org/10.1007/s10914-021-09541-0.
24. Therrien, F. (2005). Feeding behaviour and bite force of sabretoothed predators. Zool. J. Linn. Soc. *145*, 393–426. https://doi.org/10.1111/j.1096-3642.2005.00194.x.
25. Christiansen, P. (2007). Comparative bite forces and canine bending strength in feline and sabretooth felids: implications for predatory ecology. Zool. J. Linn. Soc. *151*, 423–437. https://doi.org/10.1111/j.1096-3642.2007.00321.x.
26. Christiansen, P. (2011). A dynamic model for the evolution of sabrecat predatory bite mechanics. Zool. J. Linn. Soc. *162*, 220–242. https://doi.org/10.1111/j.1096-3642.2010.00675.x.
27. McHenry, C.R., Wroe, S., Clausen, P.D., Moreno, K., and Cunningham, E. (2007). Supermodeled sabercat, predatory behavior in *Smilodon fatalis* revealed by high-resolution 3D computer simulation. Proc. Natl. Acad. Sci. USA *104*, 16010–16015. https://doi.org/10.1073/pnas.0706086104.
28. Wroe, S. (2008). Cranial mechanics compared in extinct marsupial and extant African lions using a finite-element approach. J. Zool. *274*, 332–339. https://doi.org/10.1111/j.1469-7998.2007.00389.x.
29. Wroe, S., Chamoli, U., Parr, W.C.H., Clausen, P., Ridgely, R., and Witmer, L. (2013). Comparative biomechanical modeling of metatherian and placental saber-tooths: a different kind of bite for an extreme pouched predator. PLoS One *8*, e66888. https://doi.org/10.1371/journal.pone.0066888.
30. Andersson, K., Norman, D., and Werdelin, L. (2011). Sabretoothed carnivores and the killing of large prey. PLoS One *6*, e24971. https://doi.org/10.1371/journal.pone.0024971.
31. DeSantis, L.R.G., Schubert, B.W., Scott, J.R., and Ungar, P.S. (2012). Implications of diet for the extinction of saber-toothed cats and American lions. PLoS One *7*, e52453. https://doi.org/10.1371/journal.pone.0052453.
32. Werdelin, L., McDonald, H.G., and Shaw, C.A. (2018). Smilodon: The Iconic Sabertooth (JHU Press).
33. M Janis, C.M., Figueirido, B., DeSantis, L., and Lautenschlager, S. (2020). An eye for a tooth: *Thylacosmilus* was not a marsupial "saber-tooth predator". PeerJ *8*, e9346. https://doi.org/10.7717/peerj.9346.
34. Chatar, N., Fischer, V., and Tseng, Z.J. (2022). Many-to-one function of cat-like mandibles highlights a continuum of sabre-tooth adaptations. Proc. Biol. Sci. *289*, 20221627. https://doi.org/10.1098/rspb.2022.1627.

35. Chatar, N., Michaud, M., Tamagnini, D., and Fischer, V. (2024). Evolutionary patterns of cat-like carnivorans unveil drivers of the saber-tooth morphology. Curr. Biol. *34*, 2460–2473.e4. https://doi.org/10.1016/j.cub.2024.04.055.

36. Figueirido, B., Tucker, S., and Lautenschlager, S. (2024). Comparing cranial biomechanics between Barbourofelis fricki and Smilodon fatalis: Is there a universal killing-bite among saber-toothed predators? Anat. Rec. (Hoboken). https://doi.org/10.1002/ar.25451.

37. Shelbourne, C.D., and Lautenschlager, S. (2024). Morphological diversity of saber-tooth upper canines and its functional implications.. Published online April 13, 2024. Anat. Rec. (Hoboken). https://doi.org/10.1002/ar.25458.

38. Deutsch, A.R., Berger, A., Martens, L.L., Witt, B.R., Smith, R.L.J., and Hartstone-Rose, A. (2024). Myological and osteological approaches to gape and bite force reconstruction in Smilodon fatalis.. Published online June 28, 2024. Anat. Rec. (Hoboken). https://doi.org/10.1002/ar.25529.

39. Meachen-Samuels, J.A., and Van Valkenburgh, B. (2010). Radiographs reveal exceptional forelimb strength in the sabertooth cat, *Smilodon fatalis*. PLoS One *5*, e11412. https://doi.org/10.1371/journal.pone.0011412.

40. Meachen-Samuels, J., and Van Valkenburgh, B. (2009). Forelimb indicators of prey-size preference in the Felidae. J. Morphol. *270*, 729–744. https://doi.org/10.1002/jmor.10712.

41. Antón, M., Galobart, A., and Turner, A. (2005). Co-existence of scimitar-toothed cats, lions and hominins in the European Pleistocene. Implications of the post-cranial anatomy of *Homotherium latidens* (Owen) for comparative palaeoecology. Quat. Sci. Rev. *24*, 1287–1301. https://doi.org/10.1016/j.quascirev.2004.09.008.

42. Anyonge, W. (1996). Locomotor behaviour in Plio-Pleistocene sabre-tooth cats: a biomechanical analysis. J. Zool. *238*, 395–413. https://doi.org/10.1111/j.1469-7998.1996.tb05402.x.

43. Martín-Serra, A., Figueirido, B., and Palmqvist, P. (2014). A three-dimensional analysis of morphological evolution and locomotor performance of the carnivoran forelimb. PLoS One *9*, e85574. https://doi.org/10.1371/journal.pone.0085574.

44. Meachen-Samuels, J.A. (2012). Morphological convergence of the prey-killing arsenal of sabertooth predators. Paleobiology *38*, 1–14. https://doi.org/10.1666/10036.1.

45. Piras, P., Maiorino, L., Teresi, L., Meloro, C., Lucci, F., Kotsakis, T., and Raia, P. (2013). Bite of the cats: relationships between functional integration and mechanical performance as revealed by mandible geometry. Syst. Biol. *62*, 878–900. https://doi.org/10.1093/sysbio/syt053.

46. Van Valkenburgh, B.V., and Ruff, C.B. (1987). Canine tooth strength and killing behaviour in large carnivores. J. Zool. *212*, 379–397. https://doi.org/10.1111/j.1469-7998.1987.tb02910.x.

47. Ewer, R.F. (1968). Ethology of Mammals (Logos Press Limited).

48. Sunquist, M., and Sunquist, F. (2002). Wild Cats of the World (University of Chicago Press).

49. Freeman, P.W., and Lemen, C.A. (2007). The trade-off between tooth strength and tooth penetration: predicting optimal shape of canine teeth. J. Zool. *273*, 273–280. https://doi.org/10.1111/j.1469-7998.2007.00325.x.

50. Evans, A.R., and Pineda-Munoz, S. (2018). Inferring Mammal Dietary Ecology from Dental Morphology. In Methods in Paleoecology: Reconstructing Cenozoic Terrestrial Environments and Ecological Communities, D.A. Croft, D.F. Su, and S.W. Simpson, eds. (Springer International Publishing), pp. 37–51. https://doi.org/10.1007/978-3-319-94265-0_4.

51. Quan, H., Liang, X., Zhang, X., Meyers, M.A., McMeeking, R.M., and Arzt, E. (2024). The shape of Nature's stingers revealed. Proc. Natl. Acad. Sci. USA *121*, e2316320121. https://doi.org/10.1073/pnas.2316320121.

52. Shoval, O., Sheftel, H., Shinar, G., Hart, Y., Ramote, O., Mayo, A., Dekel, E., Kavanagh, K., and Alon, U. (2012). Evolutionary trade-offs, Pareto optimality, and the geometry of phenotype space. Science *336*, 1157–1160. https://doi.org/10.1126/science.1217405.

53. Tendler, A., Mayo, A., and Alon, U. (2015). Evolutionary tradeoffs, Pareto optimality and the morphology of ammonite shells. BMC Syst. Biol. *9*, 12. https://doi.org/10.1186/s12918-015-0149-z.

54. Deakin, W.J., Anderson, P.S.L., den Boer, W., Smith, T.J., Hill, J.J., Rücklin, M., Donoghue, P.C.J., and Rayfield, E.J. (2022). Increasing morphological disparity and decreasing optimality for jaw speed and strength during the radiation of jawed vertebrates. Sci. Adv. *8*, eabl3644. https://doi.org/10.1126/sciadv.abl3644.

55. Kurten, B. (2017). Pleistocene Mammals of Europe (Routledge).

56. Slater, G.J., and Friscia, A.R. (2019). Hierarchy in adaptive radiation: A case study using the Carnivora (Mammalia). Evolution *73*, 524–539. https://doi.org/10.1111/evo.13689.

57. Rovinsky, D.S., Evans, A.R., and Adams, J.W. (2021). Functional ecological convergence between the thylacine and small prey-focused canids. BMC Ecol. Evol. *21*, 58. https://doi.org/10.1186/s12862-021-01788-8.

58. Barrett, P.Z., and Hopkins, S.S.B. (2024). Mosaic evolution underlies feliform morphological disparity. Proc. Biol. Sci. *291*, 20240756. https://doi.org/10.1098/rspb.2024.0756.

59. Barrett, P.Z. (2021). The largest hoplophonine and a complex new hypothesis of nimravid evolution. Sci. Rep. *11*, 21078. https://doi.org/10.1038/s41598-021-00521-1.

60. Álvarez-Carretero, S., Tamuri, A.U., Battini, M., Nascimento, F.F., Carlisle, E., Asher, R.J., Yang, Z., Donoghue, P.C.J., and Dos Reis, M. (2022). A species-level timeline of mammal evolution integrating phylogenomic data. Nature *602*, 263–267. https://doi.org/10.1038/s41586-021-04341-1.

61. Prevosti, F.J., Turazzini, G.F., Ercoli, M.D., and Hingst-Zaher, E. (2012). Mandible shape in marsupial and placental carnivorous mammals: a morphological comparative study using geometric morphometrics. Zool. J. Linn. Soc. *164*, 836–855. https://doi.org/10.1111/j.1096-3642.2011.00785.x.

62. Pollock, T.I., Hocking, D.P., and Evans, A.R. (2024). Is a blunt sword pointless? Tooth wear impacts puncture performance in Tasmanian devil canines. J. Exp. Biol. *227*, jeb246925. https://doi.org/10.1242/jeb.246925.

63. Pollock, T.I., Panagiotopoulou, O., Hocking, D.P., and Evans, A.R. (2022). Taking a stab at modelling canine tooth biomechanics in mammalian carnivores with beam theory and finite-element analysis. R. Soc. Open Sci. *9*, 220701. https://doi.org/10.1098/rsos.220701.

64. Vincent, J.F.V. (2017). The trade-off: a central concept for biomimetics. Bioinspired Biomimetic Nanobiomater. *6*, 67–76. https://doi.org/10.1680/jbibn.16.00005.

65. Dickson, B.V., Clack, J.A., Smithson, T.R., and Pierce, S.E. (2021). Functional adaptive landscapes predict terrestrial capacity at the origin of limbs. Nature *589*, 242–245. https://doi.org/10.1038/s41586-020-2974-5.

66. Arnold, S.J. (1983). Morphology, performance and fitness. Am. Zool. *23*, 347–361. https://doi.org/10.1093/icb/23.2.347.

67. Dickson, B.V., and Pierce, S.E. (2019). Functional performance of turtle humerus shape across an ecological adaptive landscape. Evolution *73*, 1265–1277. https://doi.org/10.1111/evo.13747.

68. Tseng, Z.J., Garcia-Lara, S., Flynn, J.J., Holmes, E., Rowe, T.B., and Dickson, B.V. (2023). A switch in jaw form–function coupling during the evolution of mammals. Philos. Trans. R. Soc. Lond. B Biol. Sci. *378*, 20220091. https://doi.org/10.1098/rstb.2022.0091.

69. Polly, P.D., Stayton, C.T., Dumont, E.R., Pierce, S.E., Rayfield, E.J., and Angielczyk, K.D. (2016). Combining geometric morphometrics and finite element analysis with evolutionary modeling: towards a synthesis. J. Vertebr. Paleontol. *36*, e1111225. https://doi.org/10.1080/02724634.2016.1111225.

70. Freeman, P.W., and Weins, W.N. (1997). Puncturing ability of bat canine teeth: the tip. In Mammalogy Papers (University of Nebraska State Museum), p. 9.

71. Freeman, P.W., and Lemen, C. (2006). Puncturing ability of idealized canine teeth: edged and non-edged shanks. J. Zool. *269*, 51–56. https://doi.org/10.1111/j.1469-7998.2006.00049.x.

72. Anderson, P.S.L. (2018). Making a point: shared mechanics underlying the diversity of biological puncture. J. Exp. Biol. *221*, jeb187294. https://doi.org/10.1242/jeb.187294.

73. Crofts, S.B., Lai, Y., Hu, Y., and Anderson, P.S.L. (2019). How do morphological sharpness measures relate to puncture performance in viperid snake fangs? Biol. Lett. *15*, 20180905. https://doi.org/10.1098/rsbl.2018.0905.

74. Popowics, T.E., and Fortelius, M. (1997). On the cutting edge: tooth blade sharpness in herbivorous and faunivorous mammals. Ann. Zool. Fenn. *34*, 73–88.

75. Evans, A.R., and Sanson, G.D. (1998). The effect of tooth shape on the breakdown of insects. J. Zool. *246*, 391–400. https://doi.org/10.1111/j.1469-7998.1998.tb00171.x.

76. Hartstone-Rose, A., and Wahl, S. (2008). Using radii-of-curvature for the reconstruction of extinct South African carnivoran masticatory behavior. C. R. Palevol *7*, 629–643. https://doi.org/10.1016/j.crpv.2008.09.015.

77. Pollock, T.I., Hocking, D.P., and Evans, A.R. (2022). The killer's toolkit: remarkable adaptations in the canine teeth of mammalian carnivores. Zool. J. Linn. Soc. *196*, 1138–1155. https://doi.org/10.1093/zoolinnean/zlab064.

78. Freeman, P.W. (1992). Canine teeth of bats (Microchiroptera): size, shape and role in crack propagation. Biol. J. Linn. Soc. *45*, 97–115. https://doi.org/10.1111/j.1095-8312.1992.tb00634.x.

79. Ewer, R. (1973). The Carnivores (Cornell University Press).

80. Tseng, Z.J. (2013). Testing adaptive hypotheses of convergence with functional landscapes: a case study of bone-cracking hypercarnivores. PLoS One *8*, e65305. https://doi.org/10.1371/journal.pone.0065305.

81. Polly, P.D. (2020). Functional tradeoffs carry phenotypes across the valley of the shadow of death. Integr. Comp. Biol. *60*, 1268–1282. https://doi.org/10.1093/icb/icaa092.

82. Frazzetta, T.H. (1966). Studies on the morphology and function of the skull in the Boidae (Serpentes). Part II. Morphology and function of the jaw apparatus in *Python sebae* and *Python molurus*. J. Morphol. *118*, 217–295. https://doi.org/10.1002/jmor.1051180206.

83. Frazzetta, T.H. (1988). The mechanics of cutting and the form of shark teeth (Chondrichthyes, Elasmobranchii). Zoomorphology *108*, 93–107. https://doi.org/10.1007/BF00539785.

84. Kardong, K.V. (1980). Evolutionary patterns in advanced snakes. Am. Zool. *20*, 269–282. https://doi.org/10.1093/icb/20.1.269.

85. King, J.E. (1983). Seals of the World (British Museum (Natural History)).

86. Kajiura, S.M., and Tricas, T.C. (1996). Seasonal dynamics of dental sexual dimorphism in the Atlantic stingray *Dasyatis sabina*. J. Exp. Biol. *199*, 2297–2306. https://doi.org/10.1242/jeb.199.10.2297.

87. Simmer, J.P., Papagerakis, P., Smith, C.E., Fisher, D.C., Rountrey, A.N., Zheng, L., and Hu, J.C. (2010). Regulation of dental enamel shape and hardness. J. Dent. Res. *89*, 1024–1038. https://doi.org/10.1177/0022034510375829.

88. Kavanagh, K.D., Evans, A.R., and Jernvall, J. (2007). Predicting evolutionary patterns of mammalian teeth from development. Nature *449*, 427–432. https://doi.org/10.1038/nature06153.

89. Evans, A.R., Pollock, T.I., Cleuren, S.G.C., Parker, W.M.G., Richards, H.L., Garland, K.L.S., Fitzgerald, E.M.G., Wilson, T.E., Hocking, D.P., and Adams, J.W. (2021). A universal power law for modelling the growth and form of teeth, claws, horns, thorns, beaks, and shells. BMC Biol. *19*, 58. https://doi.org/10.1186/s12915-021-00990-w.

90. Gould, S.J., and Lewontin, R.C. (1979). The spandrels of San Marco and the Panglossian paradigm: a critique of the adaptationist programme. Proc. R. Soc. Lond. B Biol. Sci. *205*, 581–598. https://doi.org/10.1098/rspb.1979.0086.

91. Seilacher, A. (1970). Arbeitskonzept zur konstruktions-morphologie. Lethaia *3*, 393–396. https://doi.org/10.1111/j.1502-3931.1970.tb00830.x.

92. Blount, Z.D., Lenski, R.E., and Losos, J.B. (2018). Contingency and determinism in evolution: Replaying life's tape. Science *362*, eaam5979. https://doi.org/10.1126/science.aam5979.

93. Lande, R. (1976). Natural selection and random genetic drift in phenotypic evolution. Evolution *30*, 314–334. https://doi.org/10.1111/j.1558-5646.1976.tb00911.x.

94. Brocklehurst, N. (2019). Morphological evolution in therocephalians breaks the hypercarnivore ratchet. Proc. Biol. Sci. *286*, 20190590. https://doi.org/10.1098/rspb.2019.0590.

95. Balisi, M.A., and Van Valkenburgh, B. (2020). Iterative evolution of large-bodied hypercarnivory in canids benefits species but not clades. Commun. Biol. *3*, 461. https://doi.org/10.1038/s42003-020-01193-9.

96. Friscia, A.R., Borths, M.R., and Croft, D.A. (2023). Comparing the evolution of the extinct, endemic carnivorous mammals of South America and Africa (sparassodonts and hyaenodonts). In Evolution of Cenozoic Land Mammal Faunas and Ecosystems: 25 Years of the NOW Database of Fossil Mammals (Springer), pp. 59–77. https://doi.org/10.1007/978-3-031-17491-9_5.

97. Strathmann, R.R. (1978). Progressive vacating of adaptive types during the Phanerozoic. Evolution *32*, 907–914. https://doi.org/10.1111/j.1558-5646.1978.tb04643.x.

98. Van Valkenburgh, B. (1999). Major patterns in the history of carnivorous mammals. Annu. Rev. Earth Planet. Sci. *27*, 463–493. https://doi.org/10.1146/annurev.earth.27.1.463.

99. Holliday, J.A., and Steppan, S.J. (2004). Evolution of hypercarnivory: the effect of specialization on morphological and taxonomic diversity. Paleobiology *30*, 108–128. https://doi.org/10.1666/0094-8373(2004)030<0108:EOHTEO>2.0.CO;2.

100. Van Valkenburgh, B., Wang, X., and Damuth, J. (2004). Cope's rule, hypercarnivory, and extinction in North American canids. Science *306*, 101–104. https://doi.org/10.1126/science.1102417.

101. Piras, P., Silvestro, D., Carotenuto, F., Castiglione, S., Kotsakis, A., Maiorino, L., Melchionna, M., Mondanaro, A., Sansalone, G., Serio, C., et al. (2018). Evolution of the sabertooth mandible: A deadly ecomorphological specialization. Palaeogeogr. Palaeoclimatol. Palaeoecol. *496*, 166–174. https://doi.org/10.1016/j.palaeo.2018.01.034.

102. R Development Core Team (2018). R: A language and environment for statistical computing (R Foundation for Statistical Computing). http://www.R-project.org.

103. Sansalone, G., Wroe, S., Coates, G., Attard, M.R.G., and Fruciano, C. (2024). Unexpectedly uneven distribution of functional trade-offs explains cranial morphological diversity in carnivores. Nat. Commun. *15*, 3275. https://doi.org/10.1038/s41467-024-47620-x.

104. Liu, Y., Deakin, W.J., Rayfield, E.J., and Donoghue, P.C.J. (2024). Theoretical morphospace analysis of neuropteran wings reveals little evidence of optimization for flight performance. Evol. J. Linn. Soc. *3*, kzae019. https://doi.org/10.1093/evolinnean/kzae019.

105. Smith, S.M., Stayton, C.T., and Angielczyk, K.D. (2021). How many trees to see the forest? Assessing the effects of morphospace coverage and sample size in performance surface analysis. Methods Ecol. Evol. *12*, 1411–1424. https://doi.org/10.1111/2041-210X.13624.

106. Adams, D.C., Collyer, M.L., and Kaliontzopoulou, A. (2020). Geomorph: Software for geometric morphometric analyses. R package version 3.2.1. https://cran.r-project.org/package=geomorph.

107. Milla Carmona, P. (2023). morphospace: Build, Visualize and Explore Multivariate Ordinations of Shape Data. https://github.com/millacarmona/morphospace. https://millacarmona.github.io/morphospace/.

108. Paradis, E., and Schliep, K. (2019). ape 5.0: an environment for modern phylogenetics and evolutionary analyses in R. Bioinformatics *35*, 526–528. https://doi.org/10.1093/bioinformatics/bty633.

109. Revell, L.J. (2012). phytools: An R package for phylogenetic comparative biology (and other things). Methods Ecol. Evol. *3*, 217–223. https://doi.org/10.1111/j.2041-210X.2011.00169.x.

110. Beck, R.M.D., Voss, R.S., and Jansa, S.A. (2022). Craniodental Morphology and Phylogeny of Marsupials. Bull. Am. Museum Nat. Hist. *457*, 1–352. https://doi.org/10.1206/0003-0090.457.1.1.

111. Edwards, T.R., Armstrong, B.J., Birkett-Rees, J., Blackwood, A.F., Herries, A.I.R., Penzo-Kajewski, P., Pickering, R., and Adams, J.W. (2019). Combining legacy data with new drone and DGPS mapping to identify the provenance of Plio-Pleistocene fossils from Bolt's Farm, Cradle of Humankind (South Africa). PeerJ *7*, e6202. https://doi.org/10.7717/peerj.6202.

112. Werdelin, L., and Lewis, M.E. (2013). Koobi Fora Research Project Volume 7: The Carnivora (California Academy of Sciences).

113. Kumar, S., Suleski, M., Craig, J.M., Kasprowicz, A.E., Sanderford, M., Li, M., Stecher, G., and Hedges, S.B. (2022). TimeTree 5: an expanded resource for species divergence times. Mol. Biol. Evol. *39*, msac174. https://doi.org/10.1093/molbev/msac174.

114. Dumont, E.R., Grosse, I.R., and Slater, G.J. (2009). Requirements for comparing the performance of finite element models of biological structures. J. Theor. Biol. *256*, 96–103. https://doi.org/10.1016/j.jtbi.2008.08.017.

115. Bessone, L.M., Bodereau, E.F., Cabanillas, G., and Dominguez, A. (2014). Analysis of biomechanical behaviour of anterior teeth using two different methods: Finite element method and experimental tests. Engineering *6*, 1–11.

116. Rajabizadeh, M., Van Wassenbergh, S., Mallet, C., Rücklin, M., and Herrel, A. (2021). Tooth-shape adaptations in aglyphous colubrid snakes inferred from three-dimensional geometric morphometrics and finite element analysis. Zool. J. Linn. Soc. *191*, 454–467. https://doi.org/10.1093/zoolinnean/zlaa063.

117. McGhee, G.R. (2015). Limits in the evolution of biological form: a theoretical morphologic perspective. Interface Focus *5*, 20150034. https://doi.org/10.1098/rsfs.2015.0034.

118. Benazzi, S., Kullmer, O., Grosse, I.R., and Weber, G.W. (2011). Using occlusal wear information and finite element analysis to investigate stress distributions in human molars. J. Anat. *219*, 259–272. https://doi.org/10.1111/j.1469-7580.2011.01396.x.

119. Zhang, B., Baskota, B., Chabain, J.J., and Anderson, P.S.L. (2024). Curving expectations: the minimal impact of structural curvature in biological puncture mechanics. Sci. Adv. *10*, eadp8157. https://doi.org/10.1126/sciadv.adp8157.

120. McCurry, M.R., Mahony, M., Clausen, P.D., Quayle, M.R., Walmsley, C.W., Jessop, T.S., Wroe, S., Richards, H., and McHenry, C.R. (2015). The relationship between cranial structure, biomechanical performance and ecological diversity in varanoid lizards. PLoS One *10*, e0130625. https://doi.org/10.1371/journal.pone.0130625.

121. Sharp, A.C. (2015). Comparative finite element analysis of the cranial performance of four herbivorous marsupials. J. Morphol. *276*, 1230–1243. https://doi.org/10.1002/jmor.20414.

122. Nychka, D., Furrer, R., Paige, J., and Sain, S. (2021). ''fields: Tools for spatial data''. R package version 15.2. https://github.com/dnychka/fieldsRPackage.

123. Dickson, B., Pierce, S., and Greifer, N. (2023). Morphoscape: Computation and Visualization of Adaptive Landscapes. R package version 1.0.2. https://blakedickson.github.io/Morphoscape/.

Please cite this article in press as: Pollock et al., Functional optimality underpins the repeated evolution of the extreme "saber-tooth" morphology, Current Biology (2024), https://doi.org/10.1016/j.cub.2024.11.059

STAR★METHODS

KEY RESOURCES TABLE

REAGENT or RESOURCE	SOURCE	IDENTIFIER
Deposited data		
3D surface scans (extant taxa)	https://www.morphosource.org/projects/000699335	See Data S1 for complete list with specimen numbers
3D surface scans (fossil specimens)	https://www.morphosource.org/projects/000699335	See Data S1 for complete list with specimen numbers
3D surface scans (reconstructed fossil specimens)	Available upon request from the lead author Tahlia Pollock (tahliaipollock@gmail.com)	N/A
Landmark co-ordinates	Online; supplemental information + https://figshare.com/s/885d300006243f9008a0	Online; supplemental information
Specimen list with metadata	Online; supplemental information	See Data S1
3D print surface files	Online; supplemental information + https://figshare.com/s/5b1433395768f7bcdc94	Online; supplemental information
Finite element project files	Online; supplemental information + https://figshare.com/s/e11b321633f0a6309b3c	Online; supplemental information
Software and algorithm		
R Studio v4.2.1	R Core Team[102]	https://www.r-project.org
Geomagic Wrap	3D systems	https://www.3dsystems.com
Rhinoceros 5	Robert McNeel & Associates	https://www.rhino3d.com
Avizo	Thermo Fisher Scientific	https://www.thermofisher.com
3-matic	Materialise	https://www.materialise.com
Abaqus	Dassault Systémes	https://www.3ds.com
EVIDAS Essential	HBM	https://www.hbm.com
MATLAB	MathWorks Inc.	https://www.mathworks.com

EXPERIMENTAL MODEL AND SUBJECT DETAILS

Dataset

Our dataset consists of 235 canine teeth (154 upper canines and 81 lower canines) representing 95 species of mammalian carnivores. This includes 25 saber and 70 non saber-tooth species. Our saber-tooth dataset includes species from the three major families: Nimravidae (9 species), Felidae (15 species) and Thylacosmilidae (1 species) (see Data S1). Specimens were sourced from multiple institutions: USNM (Smithsonian Museum of Natural History, USA), AMNH (American Museum of Natural History, USA), YPM (Peabody Museum of Natural History), UF (Florida Museum), DNMNH (Ditsong National Museum of Natural History, South Africa), MNHN (Muséum national d'histoire naturelle, France), NHMUK (Natural History Museum UK, United Kingdom), UCMP (University of California Museum of Paleontology, USA), IVPP (Paleozoological Museum of China, Institute of Vertebrate Paleontology and Paleoanthropology, China), LACMHC (Los Angeles County Museum of Natural History Hancock Collection, USA), NHMD (Natural History Museum of Denmark, Denmark), FMNH (Field Museum of Natural History, USA), NMV (Museums Victoria, Australia), AMS (Australian Museum, Australia), TMAG (Tasmanian Museum and Art Gallery, Australia), MZRC (Monash University Zoology Research Collection, Australia), and SMNS (State Museum of Natural History Stuttgart, Germany).

Reconstruction

Several fossil canines required reconstruction; this was done in Geomagic Wrap 2015 by T.I.P. The degree of reconstruction necessary varied among specimens from none, very small, small, small-medium, medium, medium-major, to major. Depending on the level of reconstruction necessary this could include: smoothing cracks, filling crack and chips, reconstructing the tooth tip, or using part of other teeth from the same species to reconstruct those missing (see Figure S4). Given the simplicity of the structure, we are confident in the reconstructions and have provided original (MorphoSource project: Functional optimality underpins the repeated evolution of the extreme 'saber-tooth' morphology'' (link TBA)) and reconstructed surface files (upon request).

Please cite this article in press as: Pollock et al., Functional optimality underpins the repeated evolution of the extreme ''saber-tooth'' morphology, Current Biology (2024), https://doi.org/10.1016/j.cub.2024.11.059

Study rationale

Our method differs from the traditional adaptive landscape approach, which uses theoretical shapes generated from a gridded morphospace for functional analyses.[54,65,67–69,80] To assess how shape variation impacts canine tooth performance we selected a subset of empirical tooth morphologies that spanned the shape variation present in our morphospace which were subjected to functional analyses. Empirical morphologies are a better tool in this instance for several reasons, the first being the specific question we are trying to address. Here we are interested in whether the extreme saber-tooth morphologies are functionally optimal within the context of realised canine tooth shapes, not all theoretically possible canine shapes. The traditional adaptive landscape approach is useful for extrapolating beyond empirical morphologies and exploring regions of unoccupied morphospace; however, this was not our aim, and when we implemented this procedure, it caused issues akin to previous studies.[54,68,103] The tooth morphologies we are interested in testing are notably extreme in shape, and extrapolating theoretical morphologies causes issues with shape deformations. Specifically, the theoretical morphologies generated beyond the extreme empirical forms (e.g., *Barbourofelis*) self-intersected as they became more laterally compressed. Finally, theoretical shapes are abstractions of the empirical morphologies and generated from two PC axes (PC1 and PC2), as such they capture shape variation only partially. In studies on 2D structures (e.g., wings[104]) this is less of an issue; however, in 3D this issue can be exaggerated. Empirical morphologies are more faithful to the full morphological diversity present.

The subset of teeth are as follows: non saber-tooth forms *Ailuropoda melanoleuca* (USNM-258835), *Didelphis marsupialis* (USNM-578961), *Eira barbara* (USNM-461839), *Vulpes, vulpes* (NMV-C25074), *Neofelis nebulosa* (AMNH-22916), *Panthera onca* (AMNH-75462), *Panthera uncia* (AMNH-35529), *Procyon lotor* (NMNH-265610), *Sarcophilus harrisii* (NMV-C6242); and saber-tooth forms *Dinofelis barlowi* (DNMNH-TM-1542), *Smilodon populator* (NHMD-ZMK-1/1845:2553), *Homotherium crenatidens* (MNHN-PET2000a), *Barbourofelis loveorum* (UF-VP-27447), and *Thylacosmilus atrox* (FMNH-P14531). In total, fourteen empirical teeth were subjected to biomechanical tests. This subset was chosen to deal with the logistical constraints imposed by the physical component of our tests and is not expected to severely impact landscape accuracy, as previous work has shown that this can be fairly robust to sparse and uneven morphological sampling.[105]

METHOD DETAILS

3D scanning and digitisation

Multiple methods were used to scan specimens, some specimens were scanned with laser scanners: Laser Design DS-Series 2025 (CyberOptics, USA) or Creaform HandySCAN 300 with a 0.2mm resolution (Creaform, Canada), some with structured light scanners: Artec Spider or Space Spider (Artec Group, Luxembourg), and some were CT or microCT scanned (see Data S1 for full list of specimens and details). 3D polygon meshes of teeth were generated from scans in Geomagic Wrap 2015 (Geomagic, USA).

Morphometric data collection (geometric morphometrics)

Canine shape was captured via a 3D geometric morphometrics (3D GMM) approach, using an established landmark protocol from Pollock et al.[77] Full details of the protocol can be found in Pollock et al[77]; however, here we provide a summary. Tooth models were landmarked using Computer Aided Design (CAD) software Rhinoceros 5 (McNeel North America, USA). Teeth were aligned to a global coordinate system before landmarking. The landmark protocol consisted of 31 landmarks along 3 curves (3 fixed and 28 semi-landmarks) (Figure S2). Curve 1 (the anterior curve) runs down the anterior of the tooth from tip to base, Curve 2 around the base of the tooth, and Curve 3 around the midsection of the tooth (50% of the tooth height). Three fixed landmarks were placed along the anterior curve, one at the tip, one at the midpoint at 50% of the length of the curve, and one at the base. The fixed midpoint and the base landmarks were used as anchor points for the midsection and base curves, respectively. Each curve was populated with 11 evenly spaced points, which were exported as x, y, z coordinates. Analysis and visualisation of landmark coordinate data carried out using R[102] using the packages *geomorph*[106] and *morphospace*.[107] Landmark data were subjected to a Generalised Procrustes Analysis (GPA) using the gpagen function in the *geomorph* package[106] where semi-landmarks were slid using the 'curve' argument with the minimised bending energy criterion.

Phylogeny

The phylogenetic tree used in this study for visualisations was assembled from multiple subtrees: time-scaled Maximum Clade Credibility (MCC) tree of extant terrestrial Carnivora from Slater and Friscia,[56] an informal time-scaled, composite phylogeny of marsupial and carnivoran taxa from Rovinsky et al.,[57] and a time-scaled MCC tree of extant and fossil Feliformia (including nimravid and felid saber-tooths) from Barrett and Hopkins.[58] These subtrees were combined and edited using R packages *ape*[108] and *phytools*.[109] Each subtree's taxonomy was updated as needed, and then pruned to remove unnecessary taxa. The MCC Carnivora tree was used as an overall reference and as the Caniformia branch; feliforms were pruned from this tree and the necessary species replaced on the MCC Feliformia tree, as this required fewer manual alterations. Additional missing taxa were then manually added to subtrees using the bind.tip function. Subtrees were then rooted and bound together using the bind.tree function; node and tip ages were compiled from the literature,[101,110–112] PBDB (paleobiodb.org), or TimeTree 5 (timetree.org;[113]) as needed. This phylogeny was used to visualise a phylomorphospace (Figure 2) and phenogram (Figure S1) of canine tooth forms using the mspace function in the *morphospace* package.[107]

Please cite this article in press as: Pollock et al., Functional optimality underpins the repeated evolution of the extreme "saber-tooth" morphology, Current Biology (2024), https://doi.org/10.1016/j.cub.2024.11.059

Physical puncture tests

To quantify the functional metric tooth puncture force (force [N]) we undertook a series of physical puncture tests with stainless steel 3D prints of each tooth model. To create the models for 3D printing, tooth meshes were aligned to a global coordinate system in Rhinoceros 5, so that the dorsal–ventral axis (longest axis) of the tooth was parallel to the x-axis, lingual–labial axis parallel to the y-axis, and the anterior–posterior axis parallel to the z-axis in three-dimensional space (see Figure 2 in Pollock et al.[63]). Then, each mesh was chopped perpendicular to their dorsal-ventral axis at the highest point of their basal enamel-dentine boundary, which was delineated by the basal landmark of our 3DGM protocol and chosen to reflect the 'functional' length of the tooth. As our functional metrics are integrated in the downstream Pareto analysis, it is important for the models they are based on to be identical, as each metric is describing the same model. FEA has specific requirements (the force/area ratio to be the same among compared models[114]), so each tooth model was scaled to a surface area of 450 mm^2 based on previous work.[63] This was carried over to the 3D printed physical models used in our puncture experiments. To enable secure mounting and a consistent run length (total displacement) for puncture tests, all tooth models were designed to have a specialised base block and a total height of 40 mm. As the heights of each scaled tooth model varied, to achieve the desired total model height (40 mm), the base edge of each tooth model was extruded in Geomagic Wrap 2015. The amount extruded differed for each tooth and was calculated by adding the block height (22 mm) and tooth height and subtracting it from the desired model height (40 mm). For example, for *Smilodon populator* (NHMD-ZMK-1/1845:2553) tooth model (after scaling) height = 25.73 mm and extrude amount = 2.27 mm (see Figure S2 for model creation workflow which is based on Pollock et al.[62] and Data S2A for extrude amount for each tooth). It is important to note that this extruded amount was merely a logistical necessity that facilitated consistent run lengths for physical tests; puncture data beyond the length of the tooth was not analysed or interpreted. Tooth models were printed using a selective laser melting (SLM) 3D printer, the AmPro SP500 (AmPro Innovations, Australia) from stainless steel 316L metal powder at a powder layer thickness of 40 micron. To remove the inherent variability of using a biological substrate like animal tissue, we used a gelatine substrate as a food substitute, Humimin Medical Gelatine #2 (Humimic Medical, USA), with known material properties: Density ρ: 923.468 Kg/m^3, Speed of Sound: 1457.42 m/s, Young's Modulus: 0.26 MPa, Firmness: 308 g, and Needle resistance: 0.38 N (Humimic website). Gelatine #2 is used to simulate fattier tissues and also skin and muscle. A Force Tester (Instron 5982 Universal Testing Machine, Instron, USA) with a S40A 50 kg load cell (HBM, Darmstadt, Germany) was used to measure the force (N) and displacement (mm) required by each tooth model to puncture a 50 x 50 x 50 mm block of the gelatine substrate. For each test, the tooth model was secured with a clamp attached to the load cell and the substrate placed on a platform below the tooth so that there was ~1 mm between substrate and tooth tip. The experimental set-up was designed so that the tooth moved downwards into the substrate at a constant speed of 2 mm/s for a given distance of 28 mm, taking a total of 14 seconds. For all tooth models, we performed seven replicates. The force and displacement output were recorded at 10 measurements per second by the data logger program EVIDAS Essential (v. 1.3.0, HBM, Darmstadt, Germany). The load cell is reported to have a lower limit accuracy of 0.012%, meaning that values to a resolution of approximately +/- 0.05 N are interpretable.

Finite element analysis

To quantify the functional metric tooth stress (von Mises stress [MPa]) we undertook finite element analysis (FEA) using an established protocol from Pollock et al.[63] to simulate a range of feeding behaviours. Full details of the protocol can be found in Pollock et al.[63]; here we provide an overview. We undertook a range of simulations mimicking different biting scenarios, as well as pulling and shaking behaviours. The same aligned, chopped, and scaled tooth models (minus extruding) created for physical testing were used for FEA. As per Dumont et al.[114] models were scaled to the same surface area for FEA and the value of 450 mm^2 chosen for continuity with previous research.[63] Aligned and scaled models were brought into 3-matic v14.0 (Materialise, Leuven, Belgium) to be converted into volumetric mesh files of solid (continuum) linear tetrahedral elements (C3D4) of 0.2 mm before being exported to Abaqus CAE Simulia 2019 (Dassault Systémes, Velizy-Villacoublay) to set-up and run simulations. From available data of human dentine,[115,116] models were assigned isotropic, homogeneous, and linear elastic material properties values from the literature: Young's modulus (E = 18,000 MPa) and Poisson's ratio (ν = 0.31). To test whether using a single (dentine) or multiple material (dentine and enamel) model impacted tooth stresses, we ran unidirectional biting simulations with dentine only, enamel-dentine, and dentine-dentine models for two teeth: *Canis familiaris* (MZRC-Dog45) and *Smilodon populator* (NHMD-ZMK-1/1845:2553) generated from micro-CT scans (see multi-material finite element analysis section and Figure S5). As patterns of stress distribution were similar between single and multiple material models and our study focuses on the relationship between overall patterns of form-function, all subsequent simulations undertaken were single dentine material models. Following the protocol from Pollock et al.,[63] loading conditions modelled were: initial biting (BITE 2%), 'off-angle' biting (where the tip of the tooth is not perpendicular to the food [BITE 2% AP + 30, BITE 2% AP – 30, BITE 2% LL +30, BITE 2% LL - 30]), pulling where part of the tooth is already embedded in the food (PULL 50%), and shaking where part of the tooth is already embedded in the food (SHAKE 50%), where the % represents the height of the tooth loaded (Figure S2; Data S2B). For all loading conditions, a compressive force of 300 N was applied. Finite-element models were solved using the default implicit direct static solver in Abaqus.

Pareto optimality rank-ratio approach

Pareto optimality is a framework through which a set of solutions to a multi-objective problem can be analysed to identify the subset of those solutions that can be considered optimal (the Pareto Optimal Subset (POS) or the Pareto front).[52,53,69] Members of the POS are defined as solutions against which no other solution exists in the total set with greater performance in all objectives at once. Note, given a specific weighted formula for the value of each performance objective, which can be used to measure the total value of each

solution, only a single solution in the POS would be optimal. Thus, the POS can be considered the set of all optimal solutions given any, or an unknown, relative preference for each performance objective. In the context of evolutionary biology, this is advantageous as it can test hypotheses of optimality for some trade-off without having to assume or estimate a weighting function for each performance objective. Pareto optimality therefore represents a discrete, binary characterisation of a set of solutions (those that are optimal, and those that are suboptimal). Given the variety of biological factors that bias the evolution of morphology, we do not expect biological structures to be optimal within a trade-off, only to approach it.[90,91,117] To measure biological optimality, a metric for the proximity of these solutions to the POS in performance space is required. Performance space is rarely built with comparable functional axes, as is the case in this study where we measure the breakage resistance in units of stress, and the puncture performance in units of force, both with dramatically different scales. Performance space is therefore non-Euclidean, and a non-Euclidean distance metric is needed. Because of this, some multi-objective optimization formulas have utilised (or modified) a Goldberg ranking system. Goldberg Pareto ranking is an iterative algorithm which identifies the POS of a set of solutions, assigns each solution in the POS a rank of 0, removes the POS from the set, then identifies the POS of this new set, assigns it a rank of 1, and so on until all solutions in the set are ranked. As with any rank-based solution, it has issues associated with the sampling density, as ranks will be higher for solutions with more nearby neighbours than for solutions with fewer neighbours. When identifying optimality within regions of morphospace, sampled performance spaces often have heterogeneous occupation density, which exacerbates this issue. Therefore, Deakin et al.[54] develop a Pareto Rank Ratio (PRR), which utilises two Goldberg rankings of a set of solutions: an optimal ranking, R_O, which is the original Goldberg rank; and a suboptimal ranking, R_S, which is a Goldberg ranking operated on the reversed functional performance data (usually by multiplying each metric by -1 and performing a Goldberg rank). These can then be combined in a ratio using this formula:

$$PRR = \frac{R_S}{R_O + R_S}$$

If R_O and $R_S = 0$, then the PRR is set to 1. This will happen at the end points of the POS in each sample, and when sample sizes are very small. The PRR will always be a value from 0 to 1, with 0 denoting those solutions that are maximally suboptimal (no solution is worse than them) and 1 denoting those solutions that are Pareto optimal (no solution is better than them). Ranks in between will represent the proximity to the front compared to other solutions close by.

Tooth sharpness

Tooth tip sharpness was quantified in Rhinoceros 5 for each 3D model created for performance testing based on the protocol from Pollock et al.[62] We calculated tip sharpness as: surface area of the tip of the tooth at a distance of 5 mm from the tip of the tooth. As the tooth models were already scaled to the same surface area for puncture testing and FEA, we used absolute sharpness values for comparisons between models. All sharpness measurements can be found in Data S3. We note that our 3D geometric morphometrics landmarking protocol does not capture tip sharpness, due to landmark resolution, but we include it here as a point of interest.

Multi-material finite element analysis

To test whether single (dentine only) or multiple (dentine and enamel) tooth material models impacted the patterns of stress observed we selected two exemplar teeth for which microCT scan data was available (*Canis familiaris* MZRCDog45 and *Smilodon populator* NHMD-ZMK-1/1845:2553) and performed the same biting simulations (BITE 2%). *S. populator* represents a tooth with a thin enamel layer and *C. familiaris* one with a comparatively thicker enamel layer.

As the *S. populator* tooth was broken (see Figure S4) reconstruction was necessary to model the enamel and dentine layers. To accurately model the enamel layer, measurements of the enamel thickness at multiple points along the broken tooth were taken (approximately 1/3 tooth height: posterior edge = 233 micron and labial edge = 185 micron, 1/2 tooth height: posterior edge = 238 micron and labial edge = 171 micron, and 2/3 tooth height: posterior edge = 260 micron and labial edge = 183 micron) in Avizo (Thermo Fisher Scientific, USA) from the microCT scan. These values were averaged to get a single value of 211 microns for enamel thickness. The surface(s) of the broken *S. populator* tooth were combined in Geomagic Wrap 2015 (Geomagic, USA) to create a single surface mesh reconstruction, which was used to create a multi-layer model. To do this the original surface was offset inwards 211 micron to mimic the interface between the enamel and dentine layers. From this, two new surface meshes were created that represent the enamel and dentine layers.

Teeth were microCT scanned (see Data S1 for machine details) and the enamel and dentine layers segmented out in Avizo and exported as.stl files. For this test, teeth were not scaled to the same surface area of 450 mm^2 (as per protocol for main study), they remained their original size: *C. familiaris* = 433 mm^2 and *S. populator* = 9,800 mm^2. The total force (N) applied to each tooth was scaled instead so that it was equivalent to 300 N for a 450 mm^2 surface. Enamel and dentine layers for each tooth were combined into a non-manifold surface mesh in 3-matic v14.0 (Materialise, Leuven, Belgium) and converted into volumetric mesh files of solid (continuum) linear tetrahedral elements (C3D4). To keep the number of elements comparable between each model, edge length varied: *C. familiaris* = 0.2 mm and *S. populator* = 1 mm. Teeth were assigned isotropic, homogeneous and linear elastic material properties values from the literature: Young's modulus (E = 18,000 MPa) and Poisson's ratio (ν = 0.31) from available data of human dentine[115,116,118] and Young's modulus (E = 84,000 MPa) and Poisson's ratio (ν = 0.30) from available data of human enamel.[118] In total there were three different versions of each tooth model for testing: (1) single layer with the material properties of dentine,

Please cite this article in press as: Pollock et al., Functional optimality underpins the repeated evolution of the extreme "saber-tooth" morphology, Current Biology (2024), https://doi.org/10.1016/j.cub.2024.11.059

(2) two layers based on tooth segmentation data both assigned the material properties of dentine, and (3) two layers based on tooth segmentation data one assigned the material properties of dentine and one the material properties of enamel.

In models with multiple materials, the interaction between dentine-dentine or dentine-enamel was modelled as a surface-surface tie contact. The same loading conditions were applied to all models (BITE 2%), which were solved using the default implicit direct static solver in Abaqus CAE Simulia 2019 (Dassault Systémes, Velizy-Villacoublay). Our results show that the pattern of stress distribution was similar among models (Figure S5). However, the magnitudes did vary. As the stress patterns did not vary greatly and our study investigates tooth biomechanics in a broad comparative context, we proceeded with single dentine material models. However, we highlight multi-material tooth biomechanics and the impact of relative enamel thickness as an interesting area for future research.

QUANTIFICATION AND STATISTICAL ANALYSIS

Canine tooth shape variation (geometric morphometrics)

Landmark data was ordinated using a Principal Components Analysis (PCA) to reduce dimensionality and visualise a morphospace showing the major axes of shape variation as principal components. This was performed using the gm.prcomp function in the *geomorph* package.[106] While our aim was to study the evolution of saber-tooth morphologies, we wanted to frame this in the more general context of the morphological diversity of mammalian puncturing teeth. Hence, the resulting ordination space (morphospace) is defined by the full canine tooth dataset (upper and lower canine teeth); however, for visualisations and downstream analyses we only use upper canine teeth or upper canine tooth species means. This strategy has a number of advantages that make the most of the information contained in our data set: 1) it ensures that the orientations of the PC axes that form the underlying morphospace capture the main directions of tooth shape variation comprehensively; 2) it allows a standardised assessment of morphological differences in terms of upper teeth shape variation; and 3) it provides a single point per species, simplifying both the projection of phylogenetic relationships into morphospace and its interpretation. Shapes representing phylogenetic nodes were calculated assuming a standard Brownian motion model of phenotypic evolution. Based on a linear regression (procD.lm in *geomorph*), we found a significant association between shape (Procrustes coordinates) and size ($\log_{10}$[Csize]) in our canine tooth dataset ($R^2 = 0.27$, $p < 0.001$).

Puncture performance

For analysis of tooth puncture performance, we calculated the maximum force (N) for each replicate and averaged them to give a single value for each model. Maximum force was calculated for a displacement equal to 10 mm for each tooth model (Data S3). This performance metric was chosen as it enabled us to focus on initial puncture as per Pollock et al.[62] and reduce tooth curvature as a factor impacting puncture performance. Unlike Pollock et al.[62] we did not calculate maximum force equal to tooth height because we were testing tooth morphologies that varied a lot in curvature. Specifically, as our puncture experiments are unidirectional, we are not able to simulate the tooth moving in an arc during biting (as it would in nature during jaw closure).[119] This means that a curved tooth, when penetrating to its full length, would artificially produce higher forces to puncture that a straight tooth of the same robustness. Calculating the maximum puncture force to a displacement of 10 mm avoids this, hence why we chose it as a metric for downstream analyses.

Breakage resistance

For analyses of tooth breakage resistance, we used a single summary value of von Mises stress (MPa) which was calculated as the 90th percentile maximum von Mises stress value for all surface nodes of a model (Data S3). This was done to avoid the influence of individual stress singularities.[16,120,121] The performance metric used as a proxy for breakage resistance in subsequent downstream analyses (Pareto optimality) was the maximum tooth stress under a unidirectional initial biting load (BITE 2%). We also tested the use of an inverse stress metric 'strength' = 1/(von Mises stress) as this has also been used in previous studies.[65,67,103] However, we found it did not impact the overall results of downstream analyses (Figure S6) and so used the raw von Mises stress values.

Performance surfaces and weighting metric

Functional metrics quantified for the subset of 14 teeth were mapped into the morphospace and used to create two separate performance surfaces, one for puncture performance and one for breakage resistance. To do this we used the *fields* package in R[122] and the default kriging method to fit a surface to each metric. These performance surfaces were used to predict functional metrics for all upper canine teeth in our dataset by extracting the surface values at each location in the morphospace that corresponds with a specific tooth. Some upper canine teeth in our dataset lay outside the bounds of the performance surface hull delineated by the subset of teeth tested (*Barbourofelis fricki, Thylacosmilus atrox* NHMUK 861, *Didelphis albiventris* USNM 121459, *Ailuropoda melanoleuca* USNM 259400, *Meles meles* USNM 171964). As these teeth lay outside the hull, their values could be less accurately predicted and so we excluded them. Both measured functional metrics and those predicted from the performance surfaces were plotted against one another (breakage stress [MPa] versus puncture performance [N]) to form a performance space of tooth forms. Predicted values do not match the measured metrics due to an artefact of the surface generation method (kriging). In some instances, the deviation is small (giant panda) and in others larger (red fox); however, for a majority of the tooth subset it is relatively small. This performance space was used to calculate our approximate weighting metric that indicated whether a particular morphology favours

Please cite this article in press as: Pollock et al., Functional optimality underpins the repeated evolution of the extreme ''saber-tooth'' morphology, Current Biology (2024), https://doi.org/10.1016/j.cub.2024.11.059

breakage resistance, puncture performance, or a trade-off between the two metrics. Our weighting metric is calculated as the angle between the x axis and the vector from the origin to each morphology's position in the performance space with the equation:

$$\alpha = atan\left(\frac{Force}{VMS}\right)$$

High values indicate that a form is favouring breakage resistance, low values that they are favouring puncture performance, and intermediate values that they are favouring the trade-off between metrics (Figure S3).

Canine tooth optimality landscape

To generate our optimality surface, we integrated our morphological and biomechanical data (represented as performance surfaces for puncture force (N) and tooth stress (MPa)) via the Pareto rank-ratio algorithm implemented in MATLAB following the protocol from Deakin et al.[54] The algorithm assigns each position in the morphospace hull a PRR value that is plotted as the z axis above the morphospace to create an optimality landscape.[54] To do this, the performance surfaces for puncture force and tooth stress were exported from R as data frames to MATLAB where they were subjected to the Pareto rank-ratio algorithm, creating a new PRR surface. The PRR surface was then exported from MATLAB to R and visualised using the image function in base R.[102]

Comparing landscape-based approaches

To test the accuracy of our weighting metric, we also employed an alternative method from Dickson et al.[65] using the R package *Morphoscape*[123] to calculate weightings of performance metrics in predefined groups. In this case we used the groups: saber-tooth and non saber-tooth (Data S1). Tooth morphologies in the saber-tooth group were weighted towards high stress and low puncture force, and so favoured puncture performance (stress = 0.85 and force = 0.15, z = 0.34) and morphologies in the non saber-tooth group, which included all other teeth, were weighted towards low stress and high puncture force and so favoured breakage resistance (stress = 0.05 and force = 0.95, z = 0.60) (Figure S3). The patterns observed among groups of the weights from this method broadly match with those observed for our weighting metric.

We also employed an alternate approach to test the accuracy of our performance surfaces and the optimality surfaces they are used to generate via the Pareto rank-ratio approach. This is because the algorithms for surface generation can vary between packages, which will impact surface topology. Hence, to determine whether our results were impacted by the package we chose (*fields*[122]) to generate performance surfaces, we also used the *Morphoscape*[123] to generate performance surfaces using the same set of metrics. The input data for both surface generation methods were the performance metrics quantified from our dataset of 14 tooth morphologies: puncture force (N), von Mises stress (MPa), and 1/(von Mises stress (MPa)). The resulting performance surfaces for each metric for both packages are shown in Figure S6 and represent one set of: puncture performance (Force (N)), breakage resistance (von Mises stress (MPa)), and strength (1/(von Mises stress (MPa)) generated in *fields*[122] and another set generated in *Morphoscape*[123] and as per the above protocol, integrated them via the Pareto rank-ratio algorithm to generate optimality surfaces shown in Figure S6.

There are subtle differences in the degree of smoothing/coarseness of surfaces for force (N) and stress (MPa) between packages; however, general patterns are maintained (Figure S6). For the resulting optimality surfaces, again there are subtle differences in the surfaces between packages, but general patterns are maintained with two general areas of higher optimality observed in the same locations. In the lower central region of the morphospace (straighter teeth that vary in robustness) and in the upper-middle left (extreme saber-tooth morphologies). Interestingly, in the *Morphoscape*[123] surface there is a mid-high region of optimality also observed in the top right of the morphospace (curved and more robust morphologies). However, when comparing the performance surfaces for 1/(von Mises stress (MPa)) between packages there is a noticeable difference in the degree of smoothing/coarseness of the surfaces, whereby the surface generated via *Morphoscape*[123] appears more smoothed than the surface generated via *fields*[122] (Figure S6). This impacts the resulting optimality surfaces, with the surface generated via *fields*[122] maintaining the general pattern seen in *fields*[122] force + stress and the *Morphoscape*[123] force + stress, while the *Morphoscape*[123] force + 1/stress shows a different pattern with a clear gradient from optimal morphologies along the lower boundary of the morphospace hull to suboptimal at the top boundary. We think this may be a result of how the algorithm employed by the *Morphoscape*[123] package treats very small values (like those generated by calculating the inverse of stress (1/(von Mises stress)).

As the same general optimality landscape pattern was maintained in all iterations but those including strength (1/(von Mises stress (MPa)) generated in the *Morphoscape* package, we went with the *fields*[122] force + stress pipeline for the manuscript results.